



HAL
open science

In-situ strain induced martensitic transformation measurement and consequences for the modeling of medium Mn stainless steels mechanical behavior

Ilusca Janeiro, Olivier Hubert, Jean-Hubert Schmitt

► **To cite this version:**

Ilusca Janeiro, Olivier Hubert, Jean-Hubert Schmitt. In-situ strain induced martensitic transformation measurement and consequences for the modeling of medium Mn stainless steels mechanical behavior. International Journal of Plasticity, inPress, 10.1016/j.ijplas.2022.103248 . hal-03600945

HAL Id: hal-03600945

<https://hal.science/hal-03600945>

Submitted on 7 Mar 2022

HAL is a multi-disciplinary open access archive for the deposit and dissemination of scientific research documents, whether they are published or not. The documents may come from teaching and research institutions in France or abroad, or from public or private research centers.

L'archive ouverte pluridisciplinaire **HAL**, est destinée au dépôt et à la diffusion de documents scientifiques de niveau recherche, publiés ou non, émanant des établissements d'enseignement et de recherche français ou étrangers, des laboratoires publics ou privés.

In-situ strain induced martensitic transformation measurement and consequences for the modeling of medium Mn stainless steels mechanical behavior

Ilusca Janeiro^{a,b,*}, Olivier Hubert^a, Jean-Hubert Schmitt^a

^a*Université Paris-Saclay, Centrale Supélec, ENS Paris-Saclay, Laboratoire de Mécanique Paris-Saclay, 91190 Gif-sur-Yvette, France*

^b*Aperam Stainless Steel Research Center, Isbergues, France*

Abstract

This work aims at studying the control of medium manganese austenitic stainless steels' mechanical behavior and austenite to martensite transformation via chemical composition. Six grades of austenitic stainless steel were cast with chemical compositions variations small enough able to keep relatively constant the stacking fault energy (SFE) value, but high enough to change the martensitic start temperature M_s . These experiments allow the effect of the martensite transformation on the mechanical behavior in tension to be compared while the austenitic mechanical behavior is almost unchanged. Tensile tests were performed at room temperature and at a low strain rate (10^{-4} s^{-1}). In-situ magnetic measurement is implemented to quantify the martensite volume fraction evolution with strain. Strain heterogeneities are detected by digital image correlation (DIC) analysis. For all grades, stress-strain curves exhibit Portevin-le-Châtelier (PLC) phenomenon related to localized martensite transformation within the deformation bands. For the two most unstable alloys, a Lüders plateau is detected at the yield stress. The martensite evolution is modeled using the Olson-Cohen approach, which confirms slower kinetics for the most stable grades. Moreover, it is shown that the martensite fraction evolves linearly with stress after a stress threshold function of the austenite stability represented by M_s . The martensite volume fraction vs stress slope is constant whatever the composition. This result leads to the development of a coupled metallurgical/mechanical model which depends on a single parameter M_s related to the chemical composition.

*Corresponding author

Email address: ilusca.soares_janeiro@mines-paristech.fr (Ilusca Janeiro)

now at Mines-ParisTech, PSL-Research University, CEMEF - Centre de mise en forme des matériaux, CNRS UMR 7635, CS 10207 rue Claude Daunesse, Sophia Antipolis Cedex, France

1. Introduction

Austenitic stainless steels are widely used in various industrial sectors thanks to their high formability and good corrosion resistance. Their applications cover the food industry, industrial equipment, chemical applications, power engineering, cryogenics, building industry, etc. [1]. More recently, austenitic steels are becoming increasingly attractive to the automotive sector, which is looking for alloys combining both a large ductility and a high mechanical resistance with an ultimate tensile strength (UTS) that could achieve 1.6 GPa [2]. They allow decreasing the vehicle weight while being able to absorb a significant amount of energy in case of impact. This can be achieved since deformation mechanisms in austenite - mainly planar glide and twinning - lead to high strain-hardening. Higher characteristics can even be obtained with unstable austenitic grades like AISI 301 in which martensitic transformation occurs during deformation. Controlling the kinetics of transformation allows for optimizing the couple elongation - UTS.

In addition, it is known that adjusting the chemical composition of the alloy leads to a change of Stacking Fault Energy (SFE) that favors or un-favors strain-induced martensite formation [3]. However, this phase transformation makes unstable the mechanical behavior [4]. Controlling this martensitic transformation by precise adjustment of the composition of the alloys is therefore essential, which supposes being able to accurately assess the transformation kinetics (for example the evolution of the martensitic phase fraction) under stress. Several methods are reported in the literature that can be used for the evaluation of martensite volume fraction in unstable stainless steels (see [1, 5, 6] for comparisons between different techniques). The conventional optical or electronic microscopy observations allow a global view of the microstructure and local identification of the martensite fraction. However, they lead to inaccurate estimations since local hardening due to mechanical polishing can induce martensite transformation and thus overestimate the martensite volume fraction. X-rays diffraction is probably the most widely used method [7–10]. This technique has also been used to estimate the retained austenite volume fraction in TRIP steels [11, 12]. The martensite volume fraction is deduced from peak intensities associated with the different phases. Corrections are required to take account of the crystallographic texture and its evolution during deformation. Electron Back Scattered Diffraction (EBSD) is another interesting solution since the phase analysis is coupled with microstructure observations. The quantification remains however very local despite some recent strong improvements in the indexation, and special care has to be paid for the surface preparation to avoid any artifact. Electron or neutron diffraction can also be used. Except for neutron and high energy X-rays available in synchrotron [8–10], diffraction techniques lead only to a surface evaluation of the martensite fraction. *In-situ* evaluations during strengthening with these methods are on the other hand hardly implemented. Finally, other techniques like acoustic emission monitoring and thermal analysis are reported in the literature to follow the martensitic

transformation [5, 13].

Martensite volume fraction evaluation by magnetic monitoring has been the subject of many former studies. Indeed, the α' martensite is ferromagnetic while austenite is paramagnetic (considered non-magnetic due to a very small susceptibility). The most widely used method is probably the saturation method [14–17]: the material is magnetized using a very high magnetic strength field ($H > 1.0 \times 10^6$ A/m). The main commercial solutions are sigmometer and vibrating sample magnetometer (VSM). These methods are not suitable for *in-situ* measurements since high field usually requires high current and large bulky windings (composed of a large number of turns).

”Low” magnetic field set-up (using magnetic permeability or maximal magnetization) is preferred for *in-situ* measurements [5, 12, 15, 18]: they are based on permeameters (primary coiling ensuring magnetization and pick-up coil measuring the magnetic flux variations). Some commercial solutions like ferritescope (or feritscope) can be employed [7, 19]. Other magnetic information extracted from magnetic hysteresis (remanent induction, coercive field, incremental permeability, Barkhausen noise) can also be used [18, 20, 21]. Quantities are however not proportional to the martensite content. An accurate estimation usually requires some correction due to demagnetizing effects and usually calibration by comparisons to a full saturation situation (via high magnetic field or X-rays diffraction measurements). Relative variation is sometimes preferred [15]. Despite these defaults, the main advantage of magnetic solutions is that they can be easily implemented in a tensile machine. Their high sampling rate compared to other techniques allows for high strain-rate tests for monotonic and fatigue monitoring [22].

The main goal of this work is to study the influence of the chemical composition on the kinetics of the martensitic transformation induced by the deformation. Continuous magnetic measurements during tensile tests ensure an *in-situ* quantification of the martensite fraction evolution with respect to the strain and stress. Variations of austenite stability are obtained thanks to fluctuations in composition fluctuations of very low Ni content austenitic stainless steels. Section 2 presents the materials and experimental techniques that have been employed. Experimental results, discussion, and reference modeling are gathered in section 3. Results obtained lead to the proposition of a simple macroscopic *play* model presented in section 4. This model is built from observations of common kinetics of martensite production between grades.

2. Materials and Methods

2.1. Material and metallography characterization

Six laboratory casts of low-Ni austenitic stainless steels were prepared, by progressively increasing the total amount of alloying elements. The different compositions are given in Table 1. They refer as ”ASS xx” (ASS as Austenitic

Stainless Steel), "xx" represents the element that is modified compared to the previous grade in Table 1. Note that the Cr content of ASS Si grade is slightly lower than for the other modified grades but it does not affect the composition choice to allow the progressive increase of austenite stability.

Table 1: Chemical compositions (wt.%) of the six casts studied in this work.

Casts	Cr	Mn	N	C	Ni	Si	Cu	Mo	Nb
ASS ref.	13.52	5.75	0.1	0.13	0.41	0.56	2.13	0.017	0.11
ASS Cr	14.32	5.81	0.1	0.13	0.41	0.54	2.14	0.017	0.11
ASS Ni	14.32	5.80	0.09	0.13	1.22	0.55	2.14	0.016	0.11
ASS Cu	14.35	5.78	0.09	0.13	1.21	0.55	2.68	0.017	0.11
ASS Mn	14.28	6.52	0.09	0.12	1.37	0.54	2.74	0.016	0.11
ASS Si	14.10	6.46	0.09	0.13	1.33	1.11	2.73	0.017	0.11

Ingots were first prepared, cast, hot-rolled at austenitizing temperature, and then cold rolled to obtain 1.5mm thick sheets. The mechanical process is followed by an austenitization annealing. They were then quenched to get a full prior austenite composition.

The stability of austenite is usually evaluated by looking at the theoretical *martensite start* (Ms) temperature. Ms represents the initial temperature of the martensitic transformation, below which the phase transformation occurs. According to [23], martensite start ($^{\circ}\text{C}$) evaluation in austenitic steels follows:

$$Ms(^{\circ}\text{C}) = 545 - 330(\text{C}+\text{N}) - 14\text{Cr} - 23\text{Mn} - 13\text{Cu} - 5\text{Mo} - 13\text{Ni} - 7\text{Si} \quad (1)$$

C, N, Cr, Mn, Cu, Mo, Ni, and Si denote the weight percentage of each corresponding species. Niobium is not considered in this calculation without consequence since the niobium content is the same for all casts. It must be underlined that this temperature gives only a rough and theoretical estimation of austenite stability, but it allows to rank the casts according to the relative austenite stability (Table 2). Different other formulas are available in the literature to calculate Ms and some other authors prefer to use other indicators such as Md30 [24]. These estimations do not give the same absolute temperatures but the relative position from one grade to another is quite the same. ASS ref. exhibits the highest Ms and consequently the lowest stability. Successive increasing of nickel, copper, manganese, and silicon content increases progressively the austenite stability. Due to their actual composition (Cr, Si) we observed that Ms is very close for ASS Mn and ASS Si. All next data presented in the paper have been tabulated using this list.

The Stacking Fault Energy (SFE) estimation is more problematic. On the one hand, there are several definitions in the literature giving values that are sometimes different by an order of magnitude. On the other hand, none of these

Table 2: Martensite start (Ms) temperature and Stacking Fault Energy (SFE) of the casts studied in this work (according to [23] and [25]).

Casts	ASS ref.	ASS Cr	ASS Ni	ASS Cu	ASS Mn	ASS Si
Ms (°C)	114	100	93	86	68	67
SFE (mJ.m ⁻²)	8.7	8.9	10.3	10.3	10.8	9.2

definitions takes all the chemical elements of our study into account. Among the formulations, the one proposed by Pickering and detailed in [26] seems to refer. A new formulation (equation (2)) has recently been proposed based on the analysis of former results [25]. Among the significant species, only copper does not appear in this formula.

$$\text{SFE (mJ.m}^{-2}\text{)} = 2.2 + 1.9\text{Ni} - 2.9\text{Si} + 0.77\text{Mo} + 0.5\text{C} - 0.016\text{Cr} - 3.6\text{N} \quad (2)$$

It can be seen that the SFE value is almost constant varying between 9 and 10 mJ.m⁻² whatever the cast. Other formulations also give the same kind of small variations. Copper quantity fluctuations are also sufficiently small to consider that the SFE would remain insensitive to its inclusion.

2.2. Metallographic observations and X-rays diffraction

The experimental procedure for metallographic observations is as follows: Samples are cut and then embedded in a resin to be able to observe through the thickness and along the rolling direction. Surface preparation consists of mechanical polishing (sandpaper and diamond suspension), followed by electrochemical polishing using a 95% acetic acid and 5% perchloric acid, solution and a 33V applied voltage for 60 seconds. Beraha etchant containing 0.30 g of K₂S₂O₅, 20 ml of HCl, and 100 ml of water was used to reveal the material microstructure, for a duration of about 5 to 7 seconds.

The few X-rays diffraction measurements presented in this work have been performed using a Brücker $\theta/2\theta$ diffractometer and a Co shield ($\lambda_{K\alpha} = 0.1790$ nm - Generator Current=10 mA - Generator Voltage=30 kV) at an angular velocity of $\dot{\theta}=0.2875$ °/min.

2.3. Tensile tests

Several bone-shaped specimens as illustrated in figure 1 have been cut by electroerosion machining from $e=1.5$ mm thick sheets for both tensile testing and magnetic measurements. The double connection radius makes it possible to avoid a premature rupture in the fillet. The useful zone is of $l_0=45$ mm in length and of $d = 7$ mm in width (width and thickness defining the initial S_0 and current S cross-sections). The small width makes it possible to ensure a deformation mainly concentrated in this area. The deformation during the tests was calculated in different ways: extensometry, images correlation and also simply from the machine displacement. These techniques lead to very similar results.

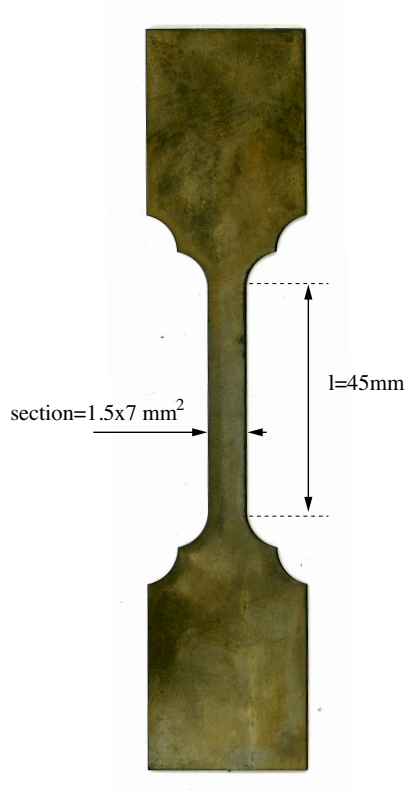


Figure 1: shape and size of the tensile test samples used in this work.

Only measurements from the machine displacement (Δl) are presented, which is consistent with the fact that the in-situ magnetic measurement system does not allow the use of another technique. All tensile tests have been performed at strain rate 10^{-4}s^{-1} using an MTS-810 displacement controlled tensile machine. Force F and the displacement Δl are recorded as functions of time allowing the plot of stress σ vs. strain ϵ curves using rational definition (equation (3)). Inelastic strain ϵ_{in} can also be evaluated (equation (3) where Y denotes the Young modulus).

$$\epsilon = \ln \left(1 + \frac{\Delta l}{l_0} \right) \quad , \quad \sigma = \frac{F}{S_0} \left(1 + \frac{\Delta l}{l_0} \right) \quad , \quad \epsilon_{in} = \epsilon - \frac{\sigma}{Y} \quad (3)$$

2.4. Digital Image Correlation

Digital Image Correlation allows the measurement of the displacement field in the full active zone (of course without magnetic set-up). This method is relevant in the case of strain localization (bands, necking) that may occur during the test. The DIC software Correli 3.0 developed at LMT has been used [27].

This technique also allows a more global deformation measurement comparable to the extensometer measurements or obtained from the machine displacement.

The first step of the calculation is to find the displacement field. This one is calculated from a comparison between the reference image and the deformed one (e.g. figure 2a) requiring a mix of black and white speckle on the surface. The DIC algorithm then locates some characteristic features on the sample surface and calculates their displacement from one image to another [28]. Each image is first separated into local areas called the *region of interest - ROI*. The displacement of each *ROI* is calculated using a grey level conservation principle between the reference configuration and the deformed configuration. DIC problem resolution is ensured by the resolution of a Finite Element formulation (mesh illustrated in figure 2b). For a more detailed presentation, readers are invited to look at the work of [29–31] and at Appendix A for a very short abstract.

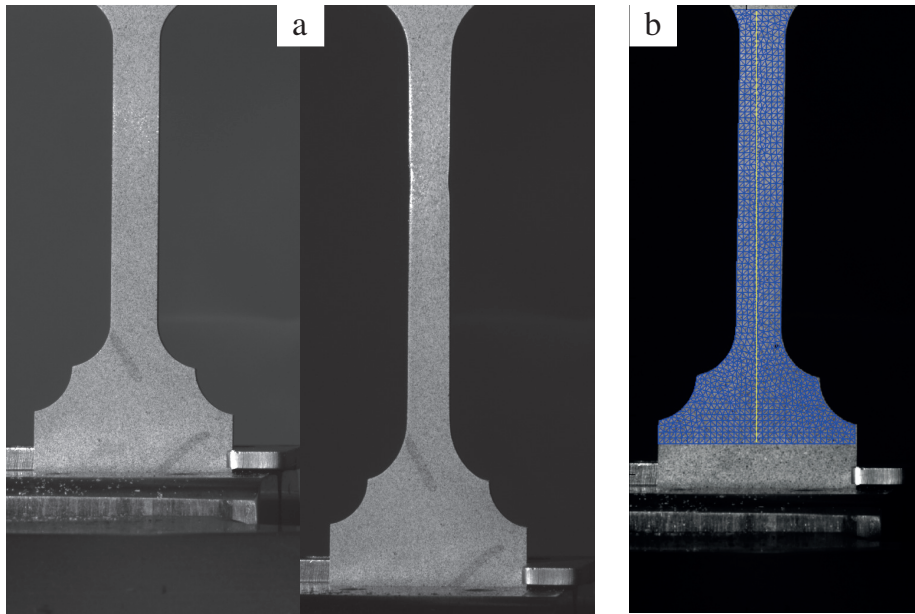


Figure 2: Illustration of pictures acquired during the tensile testing of cast ASS Cu - (a) reference image and last deformed image; (b) mesh used for DIC and virtual vertical axis (in yellow) used to extract spatio-temporal quantities.

Once the kinematic field is known for all *ROI*, the strain field can be obtained as the symmetric part of the displacement gradient. Results are sometimes noisy and convergence is sometimes hardly obtained. That's why a mechanical-based regularization has been proposed by [31]. This regularization acts as a low-pass filtering and assumes that high-frequency components of the kinematic field are most likely due to the ill-posed nature of DIC and its resolution. It

is based on the mechanical admissibility of the problem, expressed in the sense of Finite Elements interpolations. In the results presented in the next sections, regularization has only been employed to fasten the initial convergence process. Then regularization has been removed for the final convergence steps. Indeed, regularization is not suitable in the case of strongly localized deformation that tends to be smoothed.

2.5. Magnetic measurement set-up and procedure

The bench is the result of a continuous improvement of methods already presented in previous works [32–36]. Reference [12] uses a procedure for measurement of austenite volume fraction similar to the procedure we are presenting in this section. Notable improvements have however been made.

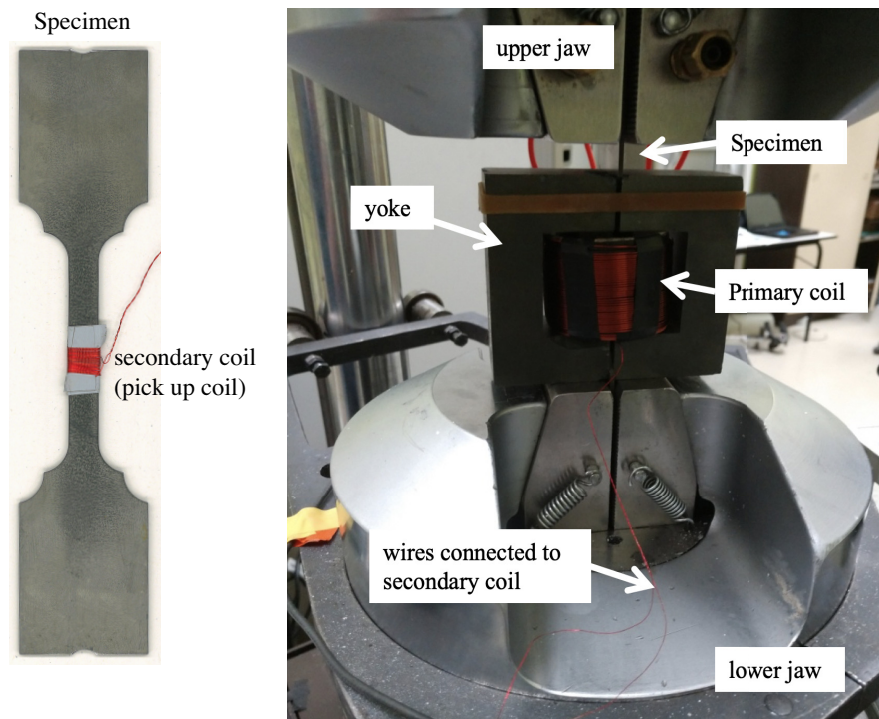


Figure 3: Apparatus for measurement of magnetic behavior during tensile test.

The benchmark for in-situ magnetic measurements is based on the principle of permeameter (figure 3). It is constituted of a primary coil made of 81 turns that allows the magnetization of the sample, and a secondary coil (pick-up coil) made of 30 turns directly wound around the samples that allows the measurement of the induced electromotive force $u(t)$. The system is current-controlled (current $i(t)$ measured by a Tektronix AMS503S current probe) by a Kepco supply driven in the primary coil by a National Instrument controller

and a home-made Labview software. Two face-to-face positioned high section ferrimagnetic U-yokes inside which the tensile specimen is positioned close to the magnetic circuit and reduce the macroscopic demagnetizing field, enhancing the magnetic field strength $H(t)$ in the material. The set-up is designed so that the heads of the specimen can be easily bitten by the jaws of the machine and so that the specimen gauge length (45mm) is higher than the inner space of the yokes (37mm) ensuring a homogeneous magnetic field strength.

The current waveform is a 2 seconds periodic signal made up of two sinusoidal cycles at the frequency of 10Hz of amplitude 7.5A followed by a pause of 1.8 seconds (see figure 4). This magnetic loading is repeated until the end of the mechanical test. The frequency of 10Hz is high enough to generate a measurable induced signal even in the absence of a ferromagnetic phase. It is low enough so that the field can be considered homogeneous throughout the thickness of the sample regardless of the amount of ferromagnetic phases in the medium. The 1.8 seconds pause allows the reduction of the input power to avoid heating the sample by the primary coiling during the strengthening (by radiation or convection).

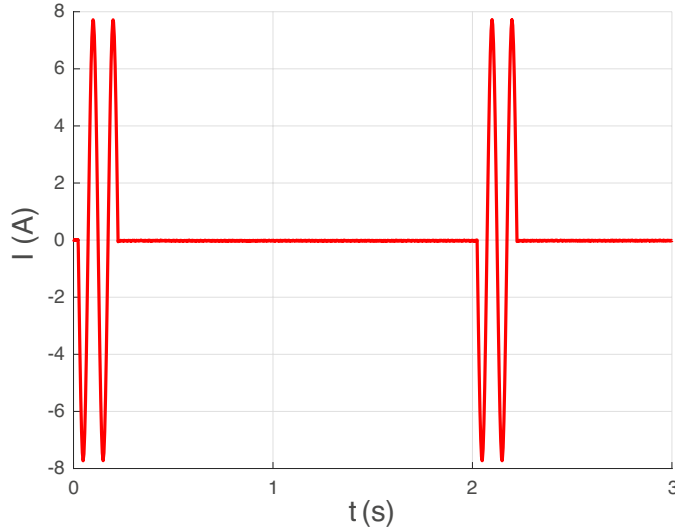


Figure 4: Typical periodic current waveform $I(t)$.

Digitizing of $i(t)$ and $u(t)$ signals is ensured by a synchronized NI-DAQ 16bit card using a 10kHz sampling frequency. Taking into account the high section ratio between the yokes and the specimen gauge and the high initial magnetic permeability of the ferrimagnetic material, the application of Ampere's theorem to the magnetic circuit formed of the specimen and the yokes makes it possible to obtain a linear relationship between the current $i(t)$ and the magnetic field $H(t)$ (equation (4)), involving the number of turns N of the primary coiling and an equivalent length l_{eq} equal in first approximation to the inner-space of

a yoke ($\approx 37\text{mm}$). On the other hand, the application of Lenz's law allows the magnetic induction $B(t)$ in the useful zone to be related to the induced voltage $u(t)$ after time integration. This relation involves the number of turns n of the secondary winding, its section S_{coil} , but also the instantaneous section of the specimen in the useful zone $S(t)$, since a part of the induced voltage is due to the magnetic field present in the space between the specimen and the coil (this magnetic field is $H(t)$ by the principle of magnetic field tangential continuity), as well as the vacuum permeability μ_0 .

$$H(t) = \frac{Ni(t)}{l_{eq}} \quad (4)$$

$$B(t) = \frac{1}{nS(t)} \int_t u(t) dt - \mu_0 H(t) \left(\frac{S_{coil}}{S(t)} - 1 \right) \quad \text{with} \quad S(t) = \frac{S_0}{1 + \frac{\Delta l}{l_0}} \quad (5)$$

The true section $S(t)$ has to be used in calculations since this section strongly varies from the beginning to the end of the tensile test. S_{coil} remains constant on the contrary. It approximately verifies $S_{coil} \approx 1.1S_0$. The magnetization $M(t)$ represents the contribution of the material to the induction. Its calculation is given by equation (6).

$$M(t) = \frac{B(t)}{\mu_0} - H(t) \quad (6)$$

It is then necessary to relate the magnetization to the martensite fraction. Several points must be considered:

- **Ferromagnetic source.** We must, first of all, make the assumption that there is no other source of ferromagnetic phase than martensite and that the martensite created is exclusively the α' ferromagnetic phase. Taking into account the composition of the material (medium Mn content) and according to the bibliographical sources (see [37] as a recent review), this assumption is acceptable. This was also confirmed by X-rays measurements on ASS ref. before and after straining.
- **Reference magnetization.** When the magnetic field is very high ($> 10^6$ A /m), the theoretical magnetization of a 100% ferromagnetic material is the true saturation magnetization of the medium denoted as M_{sat} (NB: do not confuse with the martensite start temperature M_s), mainly a function of the number of iron atoms in the study volume. When the measured magnetization is less than this value, the ferromagnetic phase fraction is less than 1. The volume fraction of the ferromagnetic phase is then equal to the ratio between the measured magnetization and the saturation magnetization. This situation is encountered in commercial devices such as sigmometer or VSM (see introduction section). It is used by several authors [14–16] for the phases assay. This technique is not suitable for *in-situ* measurements given the size of the measuring devices that it

implies. The maximum magnetic field obtained by our system is of the order of 15kA/m. This value is insufficient to lead to a true saturation of the material. The maximal magnetization obtained is denoted M_{15000} . We then denote by M_{15000}^s the maximum possible magnetization in the presence of 100% ferromagnetic phase. This value is however inaccessible and requires calibration. We denote by ζ the proportionality factor between M_{15000}^s and M_{sat} . The identification of ζ is presented in the third section. At this stage, the ferromagnetic phase fraction is calculated according to:

$$f_{\alpha'} = \frac{M_{15000}}{M_{15000}^s} = \frac{M_{15000}}{\zeta M_{sat}} \quad (7)$$

The magnetization saturation M_{sat} depends on the atoms present in the alloy as indicated above. This value, therefore, varies from one grade to another and is given by the following equation which is a modified version of [38] by APERAM:

$$M_{sat} \text{ (A/m)} = 1.71 \times 10^4 (100 - 5.5C - 1.2Mn - 1.5Ni - 1.3Cr - 1.2Mo - 1.1Cu - 2.8Si) \quad (8)$$

C, Cr, Mn, Mo, Ni, Cu, and Si denote the weight percentage of each corresponding species. Niobium and nitrogen are the only two species not considered in the formula. Considering their low weight percentage on the one hand and supposing an influence not larger than the other atoms, on the other hand, the error made by not taking them into account leads to an error of less than 1% on M_{sat} value for all casts. This error is considered small enough to warrant the use of equation (8). Table 3 gathers the obtained values used in equation (7). The typical error of Sigmameter including uncertainties concerning the magnetization saturation is about ± 0.02 .

Table 3: M_{sat} (10^6 A/m) values calculated from equation (8) and the composition of the six grades

ASS ref.	ASS Cr	ASS Ni	ASS Cu	ASS Mn	ASS Si
1.21	1.20	1.18	1.17	1.15	1.13

- **Localization effect.** A ferromagnetic phase dispersed within a non-magnetic matrix behaves like a magnetic dipole. It, therefore, creates its own magnetic field around and an internal magnetic field opposite to the magnetization of the phase. The magnetic field perceived by a particle i can be estimated via a homogenization method [39–41] using a secant 1D approach. It can be expressed as a function of the external magnetic field ($H = 15\text{kA/m}$), the magnetization M_i of the particle, the average

magnetization M in the medium, and a form factor \mathcal{N} (also called *localization* factor). i can also represent the whole martensitic phase or the whole austenitic phase. The magnetic field perceived by the martensite is then expressed according to:

$$H_{\alpha'} = H + \mathcal{N}(M - M_{\alpha'}) \quad (9)$$

The magnetization M is equal to the average of the magnetizations, that is to say:

$$M = f_{\alpha'} M_{\alpha'} + (1 - f_{\alpha'}) M_{\gamma}$$

where M_{γ} is the magnetization in the austenite. The latter is almost zero, leading to:

$$M = f_{\alpha'} M_{\alpha'}$$

and

$$H_{\alpha'} = H - \mathcal{N}(1 - f_{\alpha'}) M_{\alpha'} \quad (10)$$

The magnetic field in the martensitic phase is therefore lower than the applied field while the martensite fraction does not reach high values. And lower magnetic field means lower magnetization than expected. We denote by $M_{H_{\alpha'}}$ this magnetization, that verifies $M_{H_{\alpha'}} < M_{15000}$. The estimate of the martensite fraction $f_{\alpha'}^{loc}$ is therefore reduced:

$$f_{\alpha'}^{loc} = \frac{M_{H_{\alpha'}}}{\zeta M_{sat}} < f_{\alpha'} \quad (11)$$

Several approaches are possible to link $M_{H_{\alpha'}}$ with M_{15000} . A method based on a model link between the magnetization and the initial susceptibility has been proposed in [12] assuming an ellipsoidal shape of the martensite islands in the austenitic phase. We will see in the experimental part how it is possible to consider a homogeneous field situation for this case study.

- **Magnetoelastic effect.** It is now well established that mechanical stress can change magnetic behavior [34, 40, 42–44]. This phenomenon commonly known as the Villari effect or inverse magnetostrictive effect is a hallmark of magnetoelastic coupling. In particular, the magnetization at a given magnetic field is dependent on stress. This apparent modification of magnetization can lead, as in the case of localization, to an erroneous estimate of the martensite fraction (except to estimate the fraction at constant stress, which is incompatible with in situ testing). Taking into account the stress was the subject of a detailed study by [12] which we will not repeat here. The conclusion is that the magnetization $M_{H_{\alpha'}}^{\sigma}$, measured under stress σ for a global applied field of 15kA/m must be corrected using a magnetoelastic factor η to obtain the corresponding reference magnetization at zero stress $M_{H_{\alpha'}}$. Equation 12 applies:

$$M_{H_{\alpha'}} = \frac{M_{H_{\alpha'}}^{\sigma}}{1 + \eta\sigma} \quad (12)$$

Several preliminary observations allowed us to estimate $\eta = 3.12 \times 10^{-5} \text{ MPa}^{-1}$. Mechanical tensile stress thus leads to an overestimation of the magnetization. The martensite fraction is then finally given by:

$$f_{\alpha'}^{loc} = \frac{M_{H_{\alpha'}}^{\sigma}}{\zeta M_{sat}(1 + \eta\sigma)} \quad (13)$$

3. Experimental results

3.1. Tensile tests

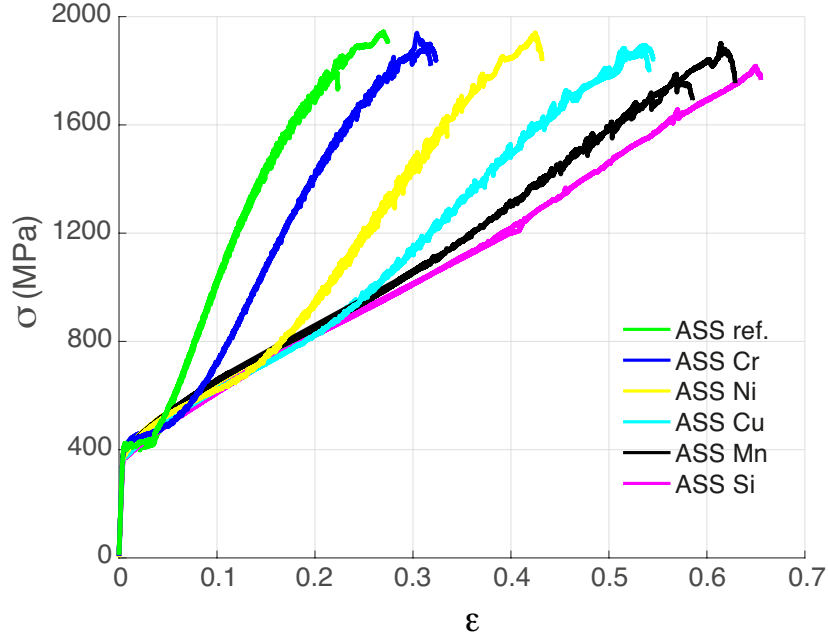


Figure 5: Stress/strain curves (σ vs ϵ) for all casts studied in this work - tests repeated two times for reproducibility purpose.

For the six grades, the stress-strain behavior in tension is nearly the same with a relatively low work-hardening at low strain, then a higher, nearly linear, hardening (Figure 5). This is particularly exemplified for the grades ASS Ni and ASS Cu. The curves for ASS ref and ASS Cr show a Lüders plateau right after the yield stress. The yield stress, roughly 380 MPa, is similar for all grades. It is seen that the more stable are the grades – that is when M_s is the lowest – the lower the strain hardening. It results that the maximum tensile stress is almost

the same whatever the grade (about 1800 MPa), but with a total elongation that grows as the austenite stability increases (from 0.27 for ASS ref to 0.65 for ASS Si). The increase of the work hardening after a few percent of deformation is associated with the induced martensitic transformation and was also early reported [45]. In a given range of temperature and strain rate, a Portevin-Le Chatelier-like (PLC) behavior is also reported (stress serrations appear for any grade at large strain during the experiments): serrations on the stress-strain curve are associated with heterogeneous deformation and deformation band propagation, as already observed for medium manganese steels [12, 46–48]. When the austenitic stainless grade is very unstable, stress-induced martensite transformation is noted within the elastic domain which leads to a transient softening after the yield stress and a Lüders plateau [45].

3.2. Optical and X-rays diffraction measurements

The induced martensitic transformation was confirmed by X-rays diffraction (XRD) and optical micrography. Figure 6 shows XRD spectra acquired for deformed and undeformed ASS ref. sample (measurement in the area of necking after plastic deformation for the deformed state). Experimental results (lines) are compared with theoretical austenite and martensite signatures (dots). Lattice parameters employed to plot theoretical points are $a_\gamma = 0.359$ nm for FCC austenite and $a_{\alpha'} = 0.2860$ nm and $c_{\alpha'} = 0.2886$ nm for QC martensite.

Conclusions are the following:

- undeformed ASS ref. is austenitic; fully deformed ASS ref. is martensitic;
- however, a weak martensite signature is detectable at the undeformed state, which may be due to sample preparation (grinding);
- a weak austenite signature is detectable at the deformed state underlining the presence of residual austenite; its volume fraction can not be accurately evaluated by this XRD technique;
- the tetragonality of martensite crystal is low with $c_{\alpha'} \approx a_{\alpha'}$ (tetragonality magnitude $(c_{\alpha'} - a_{\alpha'})/a_{\alpha'}$ is about 0.91%) leading to a weak splitting in two of BCC rays in the spectrum. This low tetragonality does not allow a preferential selection of variants with stress. This generally leads to a low stress induced transformation strain in accordance with results provided by other authors.

Optical micrography reveals that austenite first transforms along bands parallel to the rolling direction (Figure 7 for ASS ref. cast). The same kind of distribution appears for other samples. This is probably linked to a Mn-C segregation which results from casting. It leads to bands which are enriched in carbon and manganese and then are more stable. The martensite plates form within the austenite grains and leave austenite films at their interface. No accurate measurement was however performed sample by sample. Nevertheless

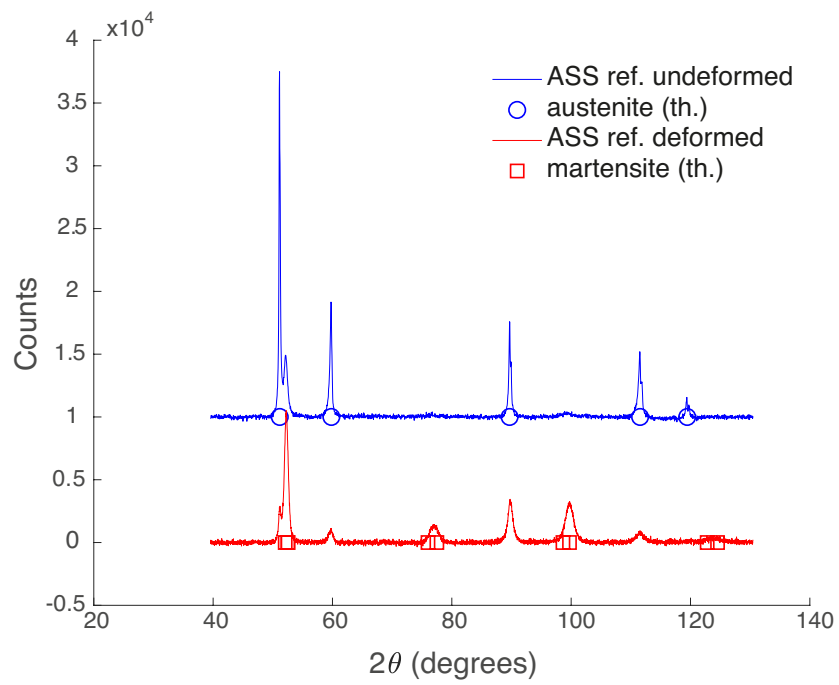


Figure 6: XRD spectrum for ASS ref. sample before and after plastic deformation - compared with theoretical austenite and and martensite signatures; spectrum for ASS ref. sample before deformation has been artificially shifted of about 10^4 counts.

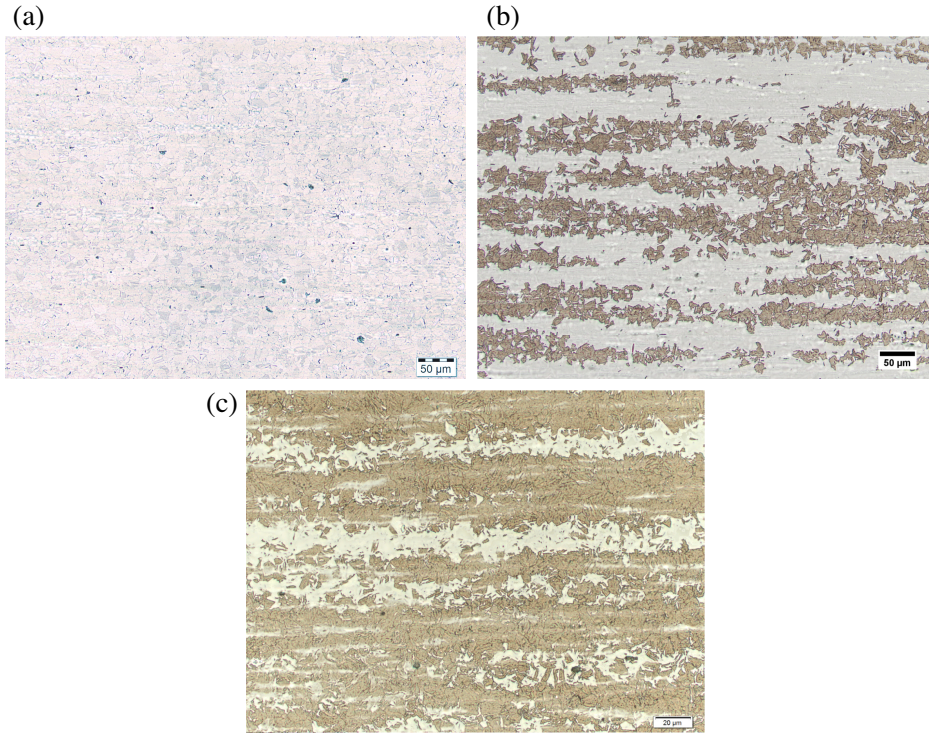


Figure 7: Typical microstructures of ASS ref. sample where martensite appears as brown islands and austenite is white : (a) fully austenitic material before deformation; (b) intermediate plastic deformation; (c) at rupture in the necking region.

these observations allow us to answer the question of the magnetic field localization (see section 2.5). The martensite bands are thus formed parallel to the applied magnetic field. A homogeneous field hypothesis can therefore in theory be applied which makes it possible to cancel the \mathcal{N} coefficient in equation (9) and to conclude that the magnetization value to be used in the calculation of martensite volume fraction is simply the measured magnetization at 15000A/m ($M_{H_{\alpha'}} \approx M_{15000}$ and $f_{\alpha'}^{loc} \approx f_{\alpha'}$).

3.3. Digital Image Correlation

One of the two mechanical tests carried out for each cast was followed by DIC. DIC measurements firstly confirm the presence of a Lüders band immediately after the yield point for the most unstable samples (ASS ref. and ASS Cr). This mechanism does not appear for the other grades. On the other hand, all grades deform by Portevin-le-Châtelier band propagation after a certain level of plastic deformation. The nucleation and the propagation of these bands correspond to the oscillations observed on the tensile curves. The strain threshold to be reached where this mechanism starts varies from one grade to another: the more stable the sample, the higher the strain threshold. It starts immediately

after the Lüders deformation for the ASS ref. and ASS Cr grades. The strain threshold is reaching about 40% for the ASS Si. The PLC mechanism start is visible on the stress-strain curves. It results in an inflection point after an almost linear hardening zone with an identical slope for most of the grades.

As for the microstructure observations, we only report the few most significant results below. They concern the ASS Cu sample, but the same observation could be carried out for other samples. Figure 8 shows an illustrative example of the PLC band propagation front at five different times. The reported measurement is the axial plastic strain rate field $\dot{\epsilon}_{yy}(\vec{x})$ calculated according to:

$$\dot{\epsilon}_{yy}(\vec{x}) = \frac{\epsilon_{yy}^{j+1}(\vec{x}) - \epsilon_{yy}^j(\vec{x})}{t^{j+1} - t^j} \quad (14)$$

j refers to a picture number. Time delay $\Delta t = t^{j+1} - t^j$ is 10s between two pictures. The strain rate is high at the front of Portevin-le-Châtellier band reaching 0.012 /s .

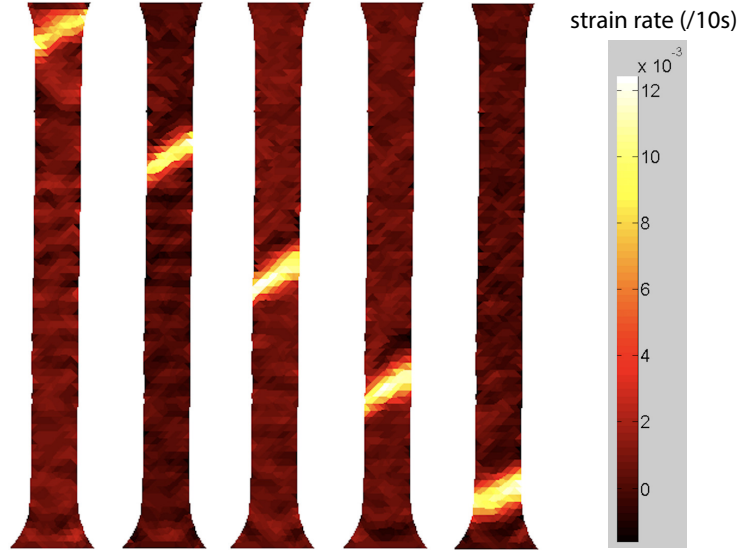


Figure 8: Bands propagation detected by DIC

Figures 9 and 10 plot a spatio-temporal evolution of the axial strain rate and axial strain for the last part of the same tensile test, respectively. The propagation speed of the bands given by the slope of the curves is relatively constant throughout the test, indicating a constant-size strain front and a constant-transported strain. The bands all initiate on the upper part of the specimen. As the necking approaches, this mechanism changes: a penultimate PLC band starts in the lower fillet. The deformation rate it carries is higher, leading to

a slower propagation speed. The last band is born in the upper fillet shortly after the arrival of the penultimate band. The front widens and the rate of deformation increases, leading to a very significant slowing down of the band up to the necking after a final direction change. These results are in agreement with those already reported in [12].

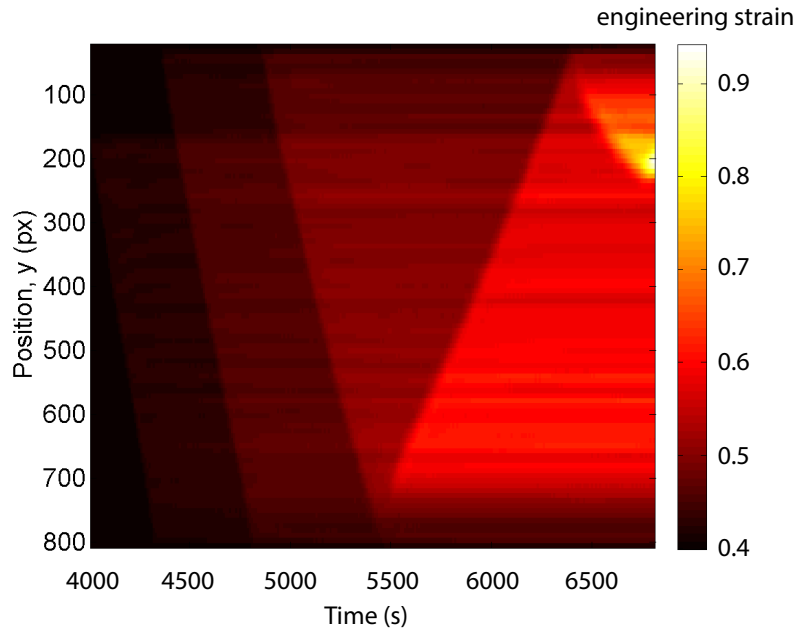


Figure 9: Spatiotemporal DIC measurements of nominal longitudinal strain of ASS Cu grade sample. The horizontal axis is the time in seconds, the vertical axis represents the position along the tensile direction, and the color bar represents total strain in the tensile direction.

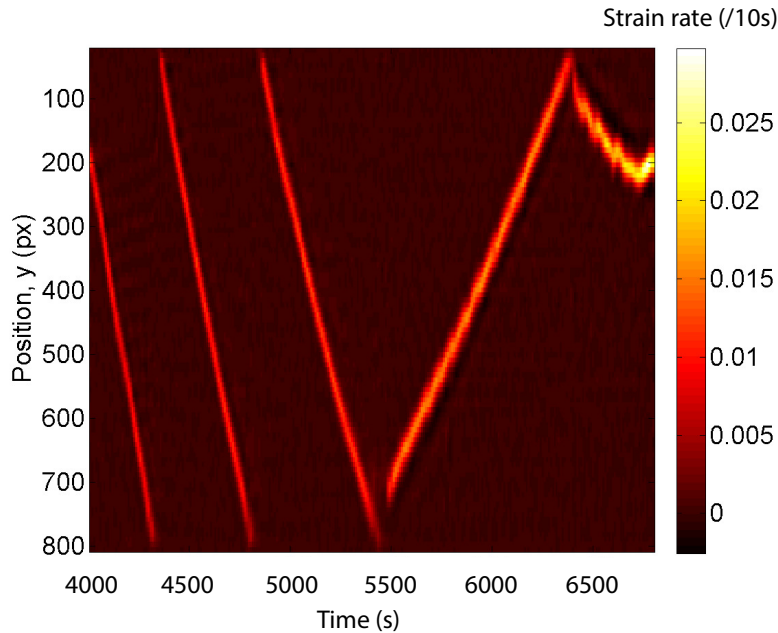


Figure 10: Spatiotemporal DIC measurements of longitudinal strain rate measurements of ASS Cu grade sample. The horizontal axis is the time in seconds, the vertical axis represents the position along the tensile direction, and the color bar represents the strain rate (1/s) in the tensile direction.

3.4. Magnetic measurements

Magnetic measurements allow us to estimate the evolution of the martensite fraction during tensile tests. They are essential for a better interpretation of the mechanical behavior and the strain fields measured by DIC. We use the results obtained for the ASS Cu grade (as for DIC) for the first illustrations.

Figure 11 illustrates first of all the magnetic hysteresis cycles obtained: as the deformation increases, an increase in the amplitude of the cycles is observed. The increase of magnetization for a given magnetic field is a direct image of the increase in the amount of ferromagnetic phase. Information contained in a cycle is numerous. We however only focus on the maximum and minimum magnetization obtained for each cycle. Figure 12a thus shows a raw measurement of the evolution of the maximum (in red) and minimum (in blue) magnetization as a function of time from the start to the end of the test carried out with ASS Cu sample. The figure shows a continuous increase in the magnitude of the magnetization over most of the duration of the test. The decrease in amplitude on the last portion of the curve corresponds to the rupture of the test piece. It mainly reflects a sudden reduction in the effective magnetic field by the appearance of an air gap in the magnetic circuit. This measurement part is therefore not usable. Figure 12b is a zoom of the previous figure for 12s. We can

observe the maximum and minimum magnetization for the 6 cycles provided. An average maximum magnetization is calculated from the norm of these two values. Results are then interpolated.

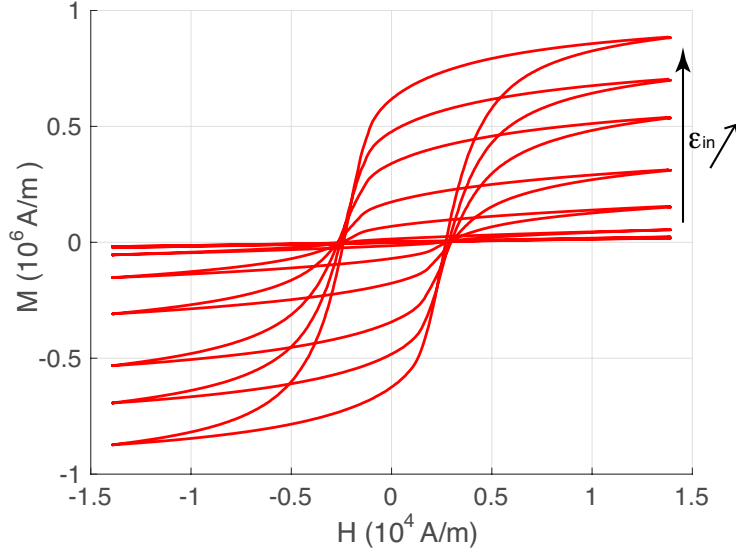


Figure 11: Evolution of magnetic hysteresis cycles with increasing inelastic strain ϵ_{in} .

Figure 13 shows a zoom of this interpolated temporal evolution. We can see a stairway variation of magnetization as a function of time. The periodicity of about 250s in the observed area corresponds to the subsequent passage of the PLC bands. Each period consists of two parts: the first part is a fast variation of magnetization. It corresponds to the moment when the front band crosses the pick-up coil. The crossing time (of the order of 30s) depends on the band speed (of the order of 0.18mm/s) and the width of the pick-up coil (of the order of 5mm). These results indicate that most of the austenite-martensite phase transformation occurs during the passage of the PLC band. The variation in magnetization measured by the sensor is thus much slower once the band has passed. The mechanism illustrated for the ASS Cu grade appears for the other grades at different strain levels. Figure 14 thus allows the comparison of the magnetization variation as a function of the inelastic deformation for all grades. This figure is a very clear illustration of the stability of a grade compared to each other. The variation in magnetization of the most stable materials (low Ms) is the lowest at a given strain. It is stronger for the less stable materials (high Ms). The stability of a grade dictates not only the evolution of the magnetization with the deformation but also the level of deformation from which this variation becomes significant, defining an increasing deformation threshold. This threshold corresponds to the end of the Lüders stage for ASS ref. and ASS Cr grades. It corresponds more or less to the inflection point observed in the stress-strain curves associated with the propagation start of the Portevin-le-Châtelier bands.

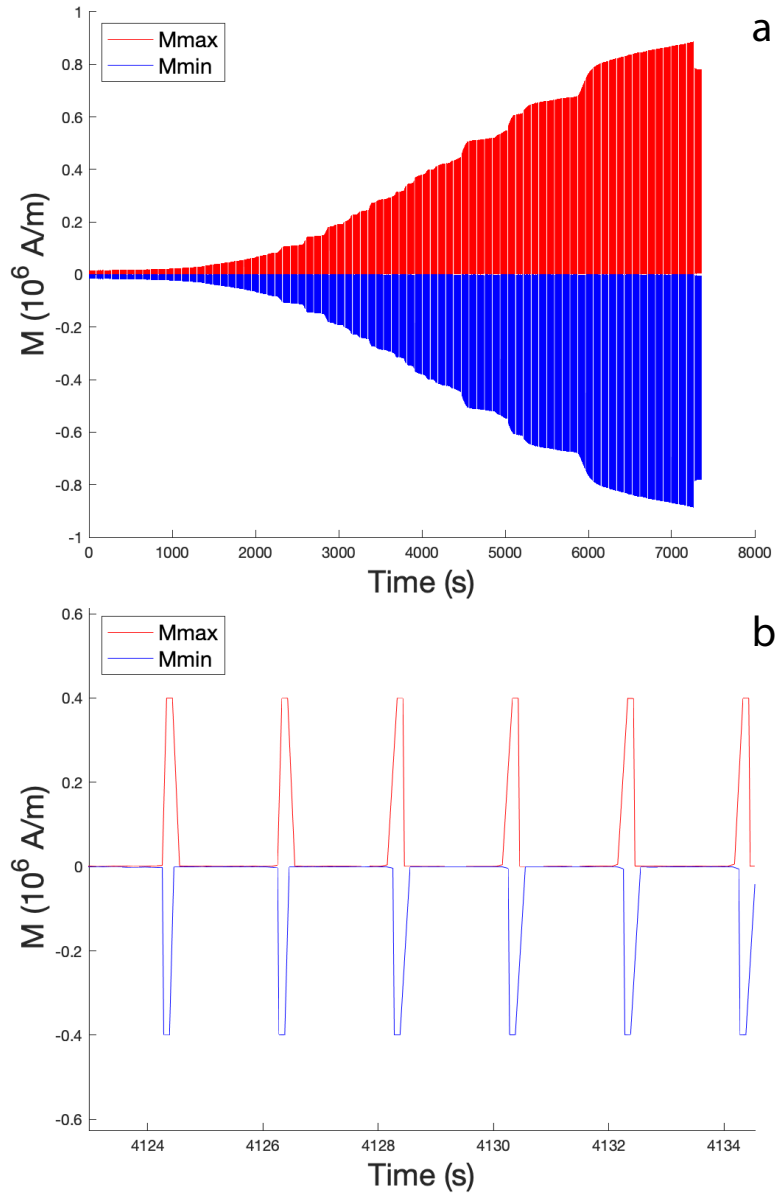


Figure 12: Evolution of maximal and minimal magnetizations.

All the curves show the fluctuations associated with the passage of these bands through the pick-up coil. The amplitude of these fluctuations seems to increase with increasing deformation. A start of magnetization saturation seems to be observed for the less stable grades. This saturation could correspond to the

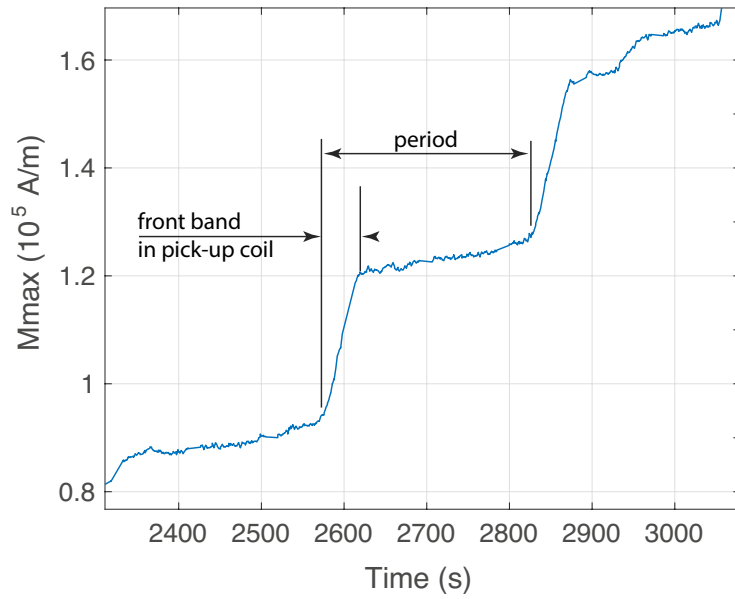


Figure 13: Evolution of maximal and minimal magnetization - interpolation

approach of a total transformation of austenite into martensite.

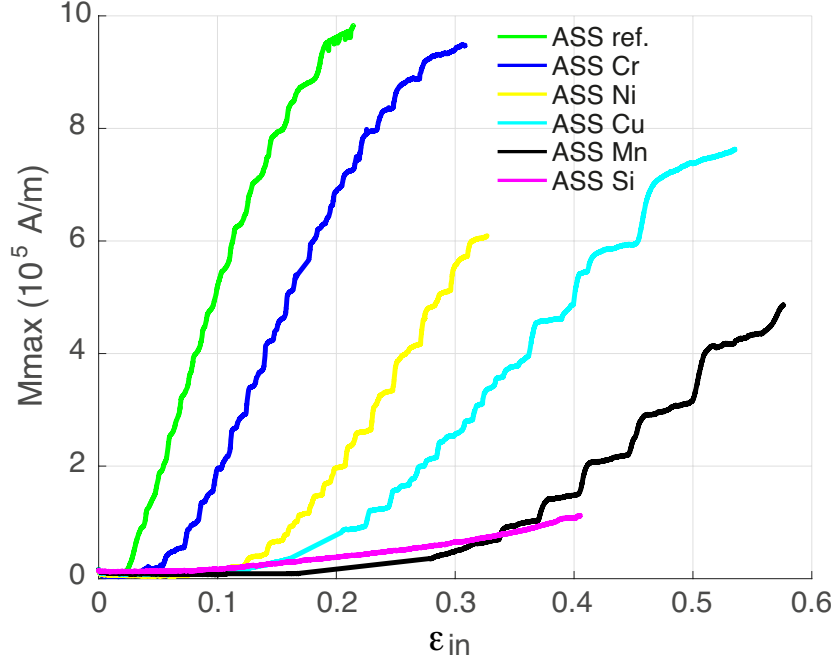


Figure 14: Evolution of magnetization as function of inelastic strain for all grades.

3.5. Extraction of martensite volume fraction and discussion

The extraction of the martensite fraction from the magnetization measurement was explained in the previous section. Equation (13) allows this calculation. We have been able to establish that, taking into account the homogeneity of the magnetic field, the measured magnetization M_{15000} can be directly used in the formula. An elastic loading-unloading mechanical test on a fully martensitic material also made it possible to evaluate the magnetoelastic parameter η . Only the ζ parameter remains unidentified. Its identification was made possible thanks to the use of a commercial Sigmameter (D6025 Sigmameter from SETARAM). Sigmameter equipment applies a magnetic field larger than 8.0×10^5 A/m over a small sample such that it reaches its saturation magnetization M_{sat}^{sigma} at zero stress (post-mortem samples are used). Equation (15) thus gives the estimate of the martensite fraction via the Sigmameter. This estimate must then correspond to the estimate given by equation (13) at the end of the test. Figure 15 then plots the evolution of $\frac{M_{15000}}{M_{sat}(1+\eta\sigma)}$ at the end of the test (measurement points correspond to the tests carried out with the six grades and tests not reported in this paper) depending on the martensite fraction measured by the Sigmameter. The error considered for experimental values

is about ± 0.04 (given mainly by uncertainties considering the magnetoelastic η parameter). We obtain a linear relation whose slope equals the dimensionless ζ constant according to equation (16). We estimate $\zeta = 0.806$.

$$f_{\alpha'} = \frac{M_{sat}^{sigma}}{M_{sat}} \quad (15)$$

$$\frac{M_{15000}}{M_{sat}(1 + \eta\sigma)} = \zeta f_{\alpha'} \quad (16)$$

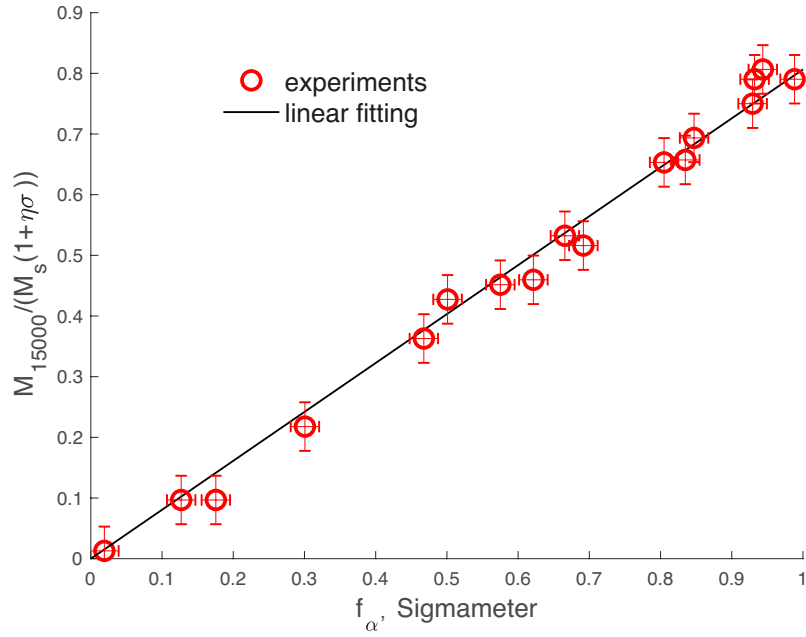


Figure 15: $\frac{M_{15000}}{M_{sat}(1+\eta\sigma)}$ vs. martensite volume fraction estimated by the commercial Sigmaster.

Curves reported in figure 16 show finally the fraction of martensite as a function of the inelastic strain $f_{\alpha'}$ vs. ϵ_i . The evolution of the fractions and the variations of magnetization, already observed and commented, are in agreement. The martensite fraction of the two most unstable grades reaches almost 100% at fracture, following a distribution law similar to a normal law. The appearance of martensite for the other grades seems to follow the same rule but the rupture prematurely interrupts the transformation more or less late depending on the grade stability. The lowest martensite evolution is obtained for the ASS Mn and ASS Si grades which have the lowest M_s value.

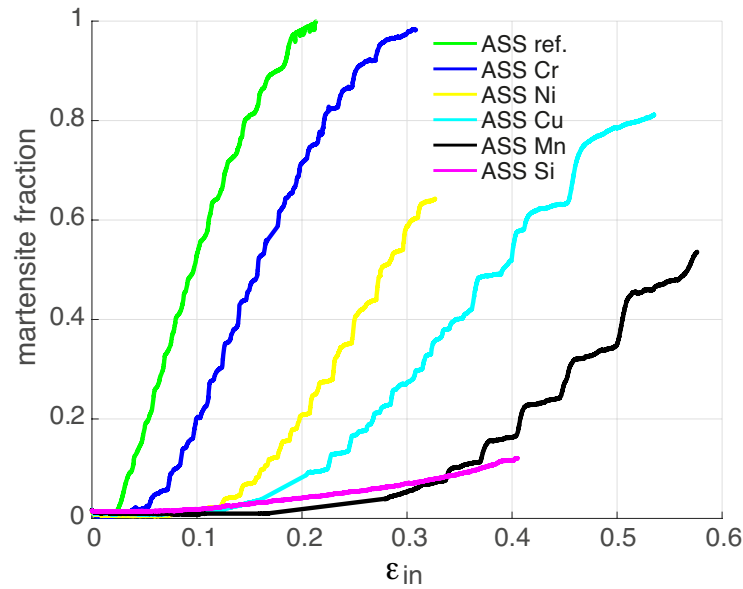


Figure 16: Martensite volume fraction as a function of inelastic strain for all grades.

For unstable austenitic stainless steels and medium Mn 3rd generation steels, it is rather usual to describe the martensite evolution as a function of strain by the Olson-Cohen model [12, 49] or its extension for stress-assisted mechanisms proposed by Stringfellow [50–52]. Olson-Cohen model applies in quasi-static condition and is given by equation (17) where α is a material parameter related to the number of shear bands and so, to the stacking fault energy of the austenite; β accounts for the probability of a martensite nucleus to form, which is in turn defined by the driving force for the phase transformation. The exponent n is usually considered constant since it describes a topological relation that relates the number of shear bands to the number of shear band intersections. In equation (17), inelastic strain ϵ_{in} is considered for simplicity reasons, even if only the plastic part should be considered. The transformation strain is negligible compared to the plastic strain part.

$$f_{\alpha'}^{OC} = (1 - \exp(-\beta(1 - \exp(-\alpha \epsilon_{in}))^n)) \quad (17)$$

A least square method was used to fit the model parameters from the martensite volume fractions measurements. The best fit is obtained when β and n values are kept constant whatever the chemical composition (Figure 17). α is then material dependent and increases when the austenite stability decreases (Table 4).

Table 4: Olson-Cohen model parameters

β	n	α ASS ref.	α ASS Cr	α ASS Ni	α ASS Cu	α ASS Mn	α ASS Si
4.5	5	12	7.9	4.1	3.1	2.0	1.7

n value is equal to 5. This value is coherent with the hypothesis by Olson and Cohen [49] assuming that the shear bands are not randomly oriented. However, since the chemical composition of the different grades is very similar, the SFE value is almost constant (Table 2). β represents the austenite stability (related to the probability for a shear band intersection to transform towards a martensite nucleus) and should be the main evolving parameter from one grade to another. However, no fitting of the experimental curves was possible while keeping α constant and varying β . The only possible way for an accurate fitting was to keep β constant ($\beta = 4.5$) and varying α , which is not in agreement with Olson and Cohen hypotheses .

Other modeling ways are available in the literature. Most of the recent models are micromechanical models based on discrete microplasticity or continuum mechanics and using a large variety of constitutive laws, some of them coming from shape memory alloys modeling. All use homogenization rules, either analytical, either numerical by finite elements [53] or using phase-field approaches [54]. There are very few macroscopic approaches proposed in the recent years.

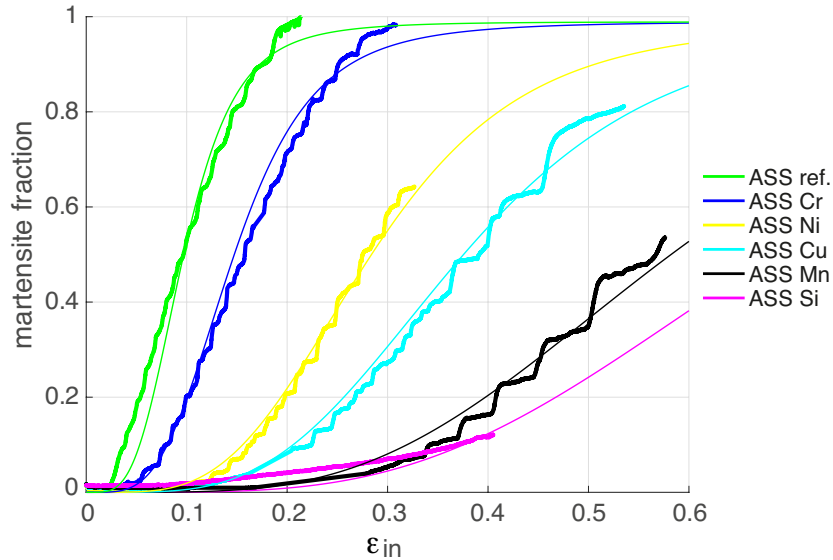


Figure 17: Martensite volume fraction as a function of inelastic strain - experiments compared with Olson-Cohen model but using constant β and variable α parameters.

They all use transformation kinetics borrowed from Olson-Cohen or alternative forms where the transformation kinetics depend on the deformation [9, 55]. The macroscopic forms of these models suppose the identification of a large number of parameters [56].

Another modeling way can however be proposed. The martensite volume fraction is plotted as a function of stress in figure 18. It is striking to see how, for five over six grades, and beyond a clear stress threshold, the variation of martensite fraction seems linearly related with the variation of stress (it must be noticed that such linearity has recently been reported in [8]). Only the ASS Si grade does not exhibit such a variation. This result is understandable given that the production of martensite did not begin for this very stable grade. This plot shows that it would be possible to model the transformation using material dependent thresholds and a single slope value. The following section gives the tools for such modeling. The advantage of such an approach is to be able to couple phase transformation and mechanical behavior in a single macroscopic model.

4. Attempt of macroscopic modeling

This section addresses the modeling of strain-induced martensite production and the stress/strain behavior as a consequence. The proposed approach partly joins that of [57] by the use of relatively simple constitutive laws for each medium. 3D thermodynamics is required to express balance equations and constitutive laws. The 3D model that can be proposed is however incomplete,

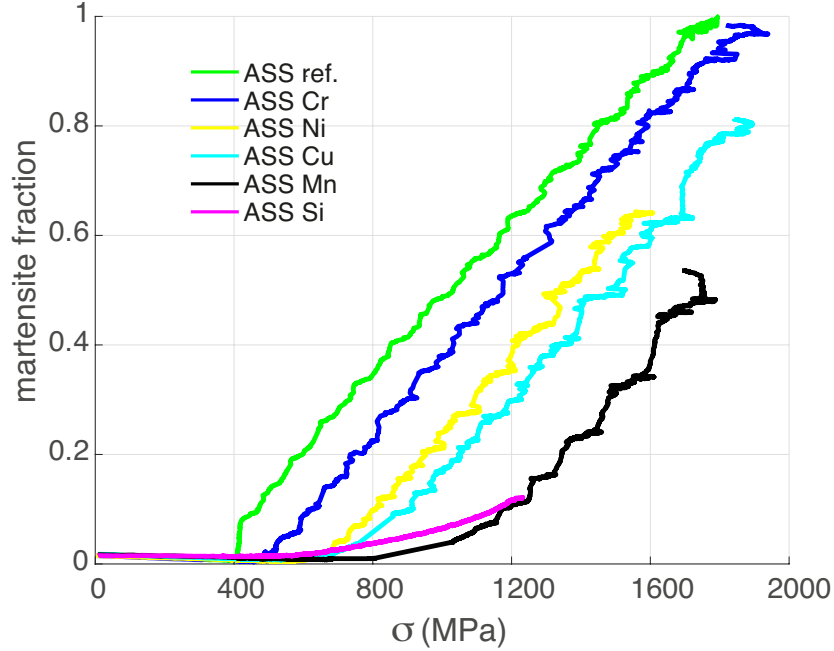


Figure 18: Martensite volume fraction as a function of stress for all grades.

missing an accurate expression of equivalent stress for phase transformation threshold. The 1D macroscopic modeling is available, allowing some interesting comparisons with 1D experiments and discussions concerning mechanisms involved in the process. Thermal effects are not addressed as well since experiments have been carried out in quasistatic conditions (meaning a global sufficient thermal exchange is considered). Thermal aspects could be considered if needed, asking for a few extensions as detailed in Appendix B. Magnetic contribution to the internal energy is not considered either. Magnetic measurement does not participate in the global equilibrium and martensite fraction rate. The reader can refer to references [34, 35] that gather the main tools required for this extension. The thermodynamics developed hereafter do not consider diffusion mechanisms either, arguing that the phase transformation is diffusion-less. Finally the modeling proposed can be considered as a simple representative volume element *play* modeling that can not address of course bands propagation or other localized phenomena.

4.1. Thermodynamics of stress/strain induced phase change

The bulk is supposed to be composed of two phases (austenite γ and martensite α') without any distinction of grains or variants. Phases do not of course remain at constant volume fraction in the proposed modeling. α' is the ferromagnetic phase. When submitted to stress, both phases are supposed to deform.

Plastic deformation of γ phase leads to strain-induced $\gamma \rightarrow \alpha'$ displacive transformation. This transformation leads on the other hand to a distortion of the lattice, at the origin of a so-called transformation strain. We propose to model the mechanism described above in this section. This modeling is built at the macroscale in the framework of irreversible processes thermodynamics and takes advantage of experimental observations. Localization phenomena observed during experiments are not considered: the modeling of a representative volume element (RVE) is looked for. Material is consequently considered as biphasic where the volume fraction of martensite (for example) can be considered as an internal variable of the macroscopic problem. The martensite volume fraction is denoted as $f_{\alpha'}$ or simply f . The austenite volume fraction is f_{γ} verifying $f_{\gamma} = 1 - f_{\alpha'} = 1 - f$.

4.1.1. Macroscopic thermodynamics

The first and second laws of thermodynamics are considered without electromagnetic power, mass transfer, and chemical reaction. They lead to the so-called Clausius-Duhem inequality (or dissipation equation)[58]:

$$\rho(T\dot{s} - \dot{u}) + \boldsymbol{\sigma} : \dot{\boldsymbol{\epsilon}} - \frac{1}{T}\mathbf{grad}T \cdot \mathbf{q}^s \geq 0 \quad (18)$$

u (J.kg⁻¹) and s (J.kg⁻¹.K⁻¹) indicate the specific internal energy and entropy densities, ρ (kg.m⁻³) is the mass density, $\boldsymbol{\sigma}$ is the stress tensor, $\boldsymbol{\epsilon}$ is the linearized strain tensor. T and \mathbf{q}^s denote the local temperature (K) and the entering heat flux (W.m⁻²).

Helmholtz free energy ψ verifies, on the other hand:

$$\psi = u - Ts \quad (19)$$

so that

$$\dot{\psi} = \dot{u} - \dot{T}s - T\dot{s} \quad (20)$$

A new formulation of the dissipation is obtained:

$$\rho(-\dot{\psi} - s\dot{T}) + \boldsymbol{\sigma} : \dot{\boldsymbol{\epsilon}} - \frac{1}{T}\mathbf{grad}T \cdot \mathbf{q}^s \geq 0 \quad (21)$$

The specific free energy density is considered as a function of elastic deformation $\boldsymbol{\epsilon}^e$ (plastic and transformation deformations are considered at the origin of purely dissipative powers), temperature, and phases volume fraction: $\psi(\boldsymbol{\epsilon}^e, T, f_i)$, so that:

$$\dot{\psi} = \frac{\partial \psi}{\partial \boldsymbol{\epsilon}^e} : \dot{\boldsymbol{\epsilon}}^e + \frac{\partial \psi}{\partial T} \dot{T} + \sum_i \frac{\partial \psi}{\partial f_i} \dot{f}_i \quad (22)$$

The total deformation rate is supposed seen as a sum of elastic, plastic $\dot{\boldsymbol{\epsilon}}^p$ and transformation $\dot{\boldsymbol{\epsilon}}^{tr}$ strain rates:

$$\dot{\boldsymbol{\epsilon}} = \dot{\boldsymbol{\epsilon}}^e + \dot{\boldsymbol{\epsilon}}^p + \dot{\boldsymbol{\epsilon}}^{tr} \quad (23)$$

Experiments showed, on one hand, that deformation occurs by a successive propagation of bands. A homogeneous stress condition can consequently be considered. This hypothesis leads to define the total strain as a contribution of each phase weighted by their volume fraction, on the other hand:

$$\boldsymbol{\epsilon} = \sum_i f_i \boldsymbol{\epsilon}_i \quad (24)$$

This equation leads to the following decomposition for strain rate:

$$\dot{\boldsymbol{\epsilon}} = \sum_i f_i \dot{\boldsymbol{\epsilon}}_i + \sum_i \dot{f}_i \boldsymbol{\epsilon}_i = \sum_i f_i (\dot{\boldsymbol{\epsilon}}_i^e + \dot{\boldsymbol{\epsilon}}_i^p + \dot{\boldsymbol{\epsilon}}_i^{tr}) + \sum_i \dot{f}_i \boldsymbol{\epsilon}_i \quad (25)$$

Equation (21) can be rewritten:

$$\rho \left(-\frac{\partial \psi}{\partial T} - s \right) \dot{T} + \left(\boldsymbol{\sigma} - \rho \frac{\partial \psi}{\partial \boldsymbol{\epsilon}^e} \right) : \dot{\boldsymbol{\epsilon}} + \sum_i \left(\boldsymbol{\sigma} : \boldsymbol{\epsilon}_i - \rho \frac{\partial \psi}{\partial f_i} \right) \dot{f}_i + \sum_i f_i \boldsymbol{\sigma} : \dot{\boldsymbol{\epsilon}}_i^p + \sum_i f_i \boldsymbol{\sigma} : \dot{\boldsymbol{\epsilon}}_i^{tr} - \frac{1}{T} \mathbf{grad} T \cdot \mathbf{q}^s \geq 0 \quad (26)$$

If we use, on the other hand, the following state laws:

$$s = -\frac{\partial \psi}{\partial T} \quad ; \quad \boldsymbol{\sigma} = \rho \frac{\partial \psi}{\partial \boldsymbol{\epsilon}^e}$$

Dissipation gives simply:

$$\sum_i f_i \boldsymbol{\sigma} : \dot{\boldsymbol{\epsilon}}_i^p + \sum_i f_i \boldsymbol{\sigma} : \dot{\boldsymbol{\epsilon}}_i^{tr} + \sum_i \left(\boldsymbol{\sigma} : \boldsymbol{\epsilon}_i - \rho \frac{\partial \psi}{\partial f_i} \right) \dot{f}_i + \frac{1}{T} \mathbf{grad} T \cdot \mathbf{q}^s \geq 0 \quad (27)$$

The first two terms refer to the plastic deformation and transformation deformation powers. The third term is a part of heat sources associated with phase fraction rate (part of latent heat phenomenon - see Appendix B). The last term is the irreversible entropy rate due to heat transfers.

4.2. Admissible constitutive law for dual-phase stainless steel

In this subsection, some constitutive laws are proposed. Our objective is not to present the most relevant or up-to-date modeling (especially for plastic strain or multiaxial situations) but show how experimental observations can be taken into account in a very simple way. We consider the following points that apply for the present study:

- the stainless steel is composed of two phases: austenite γ and martensite α' ;
- the martensite volume fraction is denoted f so that the austenite volume fraction is $1 - f$ leading to easy factorizations in equation (27);

- isothermal conditions are retained (gradients are null): the last term in equation (27) vanishes;
- transformation strain is obviously null in the austenite. It can be on the other hand considered as constant in the martensite, neglecting some possible variant selection or twinning/de-twinning mechanism. Martensite transformation deformation rate therefore verifies $\dot{\epsilon}_{\alpha'}^{tr} = \mathbf{0}$;
- Applying a mixing law to the specific Helmholtz free energy density ($\psi = \sum_i f_i \psi_i$), the partial derivative writes: $\rho \frac{\partial \psi}{\partial f_i} = \rho \psi_i$. The dissipation term associated with transformation rate can be developed as follows;

$$\sum_i \left(\boldsymbol{\sigma} : \boldsymbol{\epsilon}_i - \rho \frac{\partial \psi}{\partial f_i} \right) \dot{f}_i = \sum_i (\boldsymbol{\sigma} : \boldsymbol{\epsilon}_i - \rho \psi_i) \dot{f}_i = \sum_i -\rho \mathbf{g}_i \dot{f}_i \quad (28)$$

where \mathbf{g}_i denotes the specific Gibbs free energy density of phase i .

The Clausius-Duhem inequality is finally obtained for our problem using austenite and martensite quantities, as a simplification of the dissipation equation (27):

$$f \boldsymbol{\sigma} : \dot{\boldsymbol{\epsilon}}_{\alpha'}^p + (1-f) \boldsymbol{\sigma} : \dot{\boldsymbol{\epsilon}}_{\gamma}^p - \rho \dot{f} (\mathbf{g}_{\alpha'} - \mathbf{g}_{\gamma}) \geq 0 \quad (29)$$

The positivity of this inequality is obtained by a positivity of each term. Let us now have a look at each term separately in order to build a set of simple constitutive laws. Terms are developed for a 3D problem first:

- Plastic power in the martensite phase

$$\boldsymbol{\sigma} : \dot{\boldsymbol{\epsilon}}_{\alpha'}^p \geq 0 \quad (30)$$

This inequality is corresponding to positive dissipation in α' phase. This condition is verified using for example a Prager or Prandtl-Reuss flow rule in the framework of associate plasticity (non-associated plasticity is another possible framework allowing non-linear kinematic or isotropic strengthening [57]), considering yield stress $\sigma_{\alpha'}^y$, von Mises equivalent stress σ_{eq} , yield function \mathfrak{f} , isotropic strengthening $R_{\alpha'}$ and cumulative plastic strain $p_{\alpha'}$. The following flow rules are obtained:

$$\left\{ \begin{array}{l} \mathfrak{f}(\boldsymbol{\sigma}, R_{\alpha'}) = \sigma_{eq}(\boldsymbol{\sigma}) - \sigma_{\alpha'}^y - R_{\alpha'} \\ \text{if } \mathfrak{f} < 0, \text{ then } \dot{\boldsymbol{\epsilon}}_{\alpha'}^p = \mathbf{0} \text{ and } \dot{R}_{\alpha'} = 0 \\ \text{if } \mathfrak{f} = 0, \text{ then } \dot{\boldsymbol{\epsilon}}_{\alpha'}^p = \dot{p}_{\alpha'} \frac{d\mathfrak{f}}{d\boldsymbol{\sigma}} \text{ and } \dot{R}_{\alpha'} = k_{\alpha'} \dot{p}_{\alpha'} \end{array} \right. \quad (31)$$

with, \mathbf{s} denoting the stress deviator,

$$\sigma_{eq} = \sqrt{\frac{3}{2} \mathbf{s} : \mathbf{s}} \quad ; \quad \dot{p} = \sqrt{\frac{2}{3} \dot{\boldsymbol{\epsilon}}^p : \dot{\boldsymbol{\epsilon}}^p}$$

- Plastic power in the austenite phase

$$\boldsymbol{\sigma} : \dot{\boldsymbol{\epsilon}}_\gamma^p \geq 0 \quad (32)$$

We apply the same rule for phase γ than for α' phase defining the same set of quantities and parameters: considering yield stress σ_γ^y , von Mises equivalent stress σ_{eq} , yield function f , isotropic strengthening R_γ , and cumulative plastic strain p_γ , the following flow rules are obtained:

$$\left\{ \begin{array}{l} f(\boldsymbol{\sigma}, R_\gamma) = \sigma_{eq}(\boldsymbol{\sigma}) - \sigma_\gamma^y - R_\gamma \\ \text{if } f < 0, \text{ then } \dot{\boldsymbol{\epsilon}}_\gamma^p = \mathbf{0} \text{ and } \dot{R}_\gamma = 0 \\ \text{if } f = 0, \text{ then } \dot{\boldsymbol{\epsilon}}_\gamma^p = \dot{p}_\gamma \frac{df}{d\boldsymbol{\sigma}} \text{ and } \dot{R}_\gamma = k_\gamma \dot{p}_\gamma \end{array} \right. \quad (33)$$

- Specific Gibbs free energy density balance

$$-\rho \dot{f}(\mathbf{g}_{\alpha'} - \mathbf{g}_\gamma) \geq 0 \quad (34)$$

This equation states that martensite production occurs when the specific Gibbs free energy density of martensite is lower than the specific Gibbs free energy density of austenite. Expression of energy densities is not required, however. The linear relationship between martensite ratio and stress that has been observed experimentally once a specific yield stress (phase transformation threshold) has been overcome agrees with the positive dissipation principle.

Once the transformation threshold has been reached, the martensite production occurs. The reverse transformation is not possible. The martensite rate rule looks very close to a cumulative plastic strain. Then, as for plasticity description, we propose to define a transformation yield function f , a transformation yield stress σ_s , a linear isotropic strengthening R_m verifying:

$$\left\{ \begin{array}{l} f(\boldsymbol{\sigma}) = \sigma_{eq}(\boldsymbol{\sigma}) - \sigma_s - R_s \\ \text{if } f < 0, \text{ then } \dot{f} = 0 \\ \text{if } f = 0, \text{ then } \dot{R}_s = k_s \dot{f} \text{ until } f = 1 \end{array} \right. \quad (35)$$

Equivalent stress σ_{eq} for phase transformation would have to be defined. The reader can refer to the work of [59] where such equivalent stress has been proposed. Since only uniaxial stress conditions are met in the experimental part of the work, this point has not been developed further, by considering it out of the scope of the paper.

The transformation strain is generally considered as low even at saturation as indicated in 3.2. We propose not to take it into account for the comparison with the experiments, avoiding the identification of one more parameter.

4.3. Application to 1D monotonic loading and identification of paramaters

The previous flow rules can be written for a 1D monotonic situation as follows:

$$\left\{ \begin{array}{l} \mathfrak{f}(\sigma, R_{\alpha'}) = \sigma - \sigma_{\alpha'}^y - R_{\alpha'} \\ \text{if } \mathfrak{f} < 0, \text{ then } \dot{\epsilon}_{\alpha'}^p = 0 \\ \text{if } \mathfrak{f} = 0, \text{ then } \dot{\epsilon}_{\alpha'}^p = \frac{\dot{R}_{\alpha'}}{k_{\alpha'}} \end{array} \right. \quad (36)$$

$$\left\{ \begin{array}{l} \mathfrak{f}(\sigma, R_{\gamma}) = \sigma - \sigma_{\gamma}^y - R_{\gamma} \\ \text{if } \mathfrak{f} < 0, \text{ then } \dot{\epsilon}_{\gamma}^p = 0 \\ \text{if } \mathfrak{f} = 0, \text{ then } \dot{\epsilon}_{\gamma}^p = \frac{\dot{R}_{\gamma}}{k_{\gamma}} \end{array} \right. \quad (37)$$

$$\left\{ \begin{array}{l} \mathfrak{f}(\sigma, R_s) = \sigma - \sigma_s - R_s \\ \text{if } \mathfrak{f} < 0, \text{ then } \dot{f} = 0 \\ \text{if } \mathfrak{f} = 0, \text{ then } \dot{f} = \frac{\dot{R}_s}{k_s} \text{ until } f = 1 \end{array} \right. \quad (38)$$

These rules define 3 yield stresses and 3 strengthening constants. All parameters are *a priori* materials-dependent. However, experimental measurements have shown similarities in the behavior of the six grades, making it possible to limit the number of parameters. A correlation with the theoretical phase transformation temperature M_s can also be sought. We consider for modeling that:

- austenite yield stress σ_{γ}^y is the same for all grades;
- martensite yield stress $\sigma_{\alpha'}^y$ is the same for all grades;
- transformation threshold σ_s is different from one grade to another, obtained by a simple linear fitting of the different $f(\sigma)$ characteristics;
- martensite strengthening parameter $k_{\alpha'}$ is the same for all grades;
- austenite strengthening parameter k_{γ} is the same for all grades before the transformation threshold σ_s ;
- austenite strengthening parameter k_{γ} is different from one grade to another above the transformation threshold σ_s : it is obtained by a simple linear fitting of the different $\sigma(\epsilon)$ curves for a linear portion of about 100MPa just above σ_s . The strengthening parameter is referred as θ_s in the following.

Results are gathered in tables 5 and 6. Figures 19, 20 and 21 allow the performance of the modeling to be appreciated, by plotting experimental and modeled martensite fraction versus stress, stress-strain curves (using a Young modulus $Y = 190$ GPa), and martensite fraction versus inelastic strain. Despite the use of very simple linear strengthening relationships, experimental results and modeling are in good agreement. The model reproduces accurately the well-known supplementary work hardening after the transformation threshold. The discrepancy between the experiment and the model for ASS-ref is explained by

the fact that there is no ingredient in the model to reproduce the stress plateau. Martensite is produced at constant stress over 2% strain range. Agreement between experiment and modeling becomes satisfactory when this shift is taken into account. The model also poorly reproduces the evolution of the martensite fraction for the most stable grades. Only introducing a linear relationship between martensite fraction and stress seems finally a simple and relevant way to model the behavior of unstable medium manganese stainless steels, however. A non-associated framework for plasticity and appropriate modeling of the stress plateau would have probably led to better results but would require the identification of more parameters.

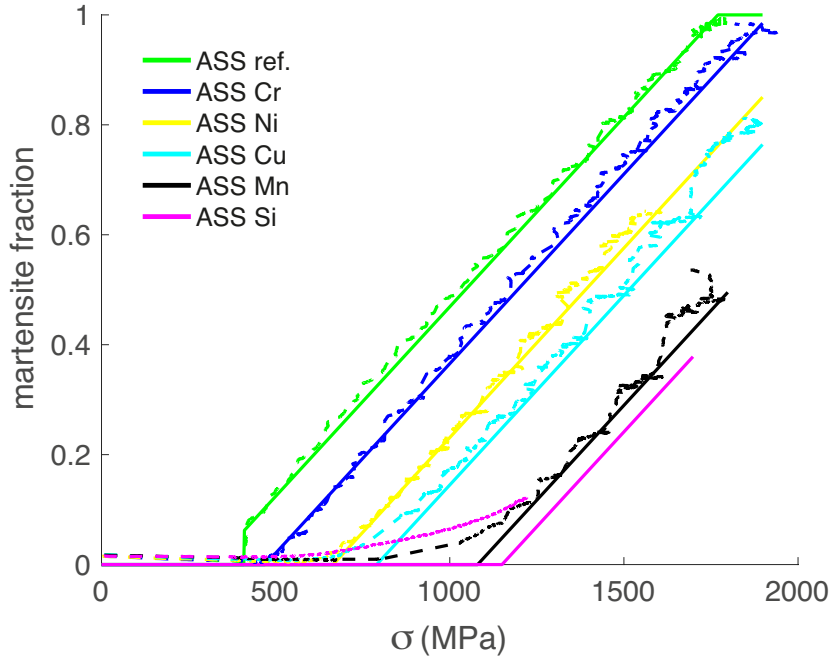


Figure 19: Martensite volume fraction as a function of stress for all grades - experimental (dashed lines) vs. modeling results

Table 5: Plastic strengthening parameters

$\sigma_{\alpha'}^y$ (MPa)	$k_{\alpha'}$ (MPa)	σ_{γ}^y (MPa)	k_{γ} (MPa)	k_s (MPa)
1600	4000	410	1900	1450

On the other hand, it looks interesting to plot the material-dependent parameters in table 6 as a function of theoretical martensite start temperature. As highlighted in figure 22, σ_s exhibits a linear variation with M_s . A least-square

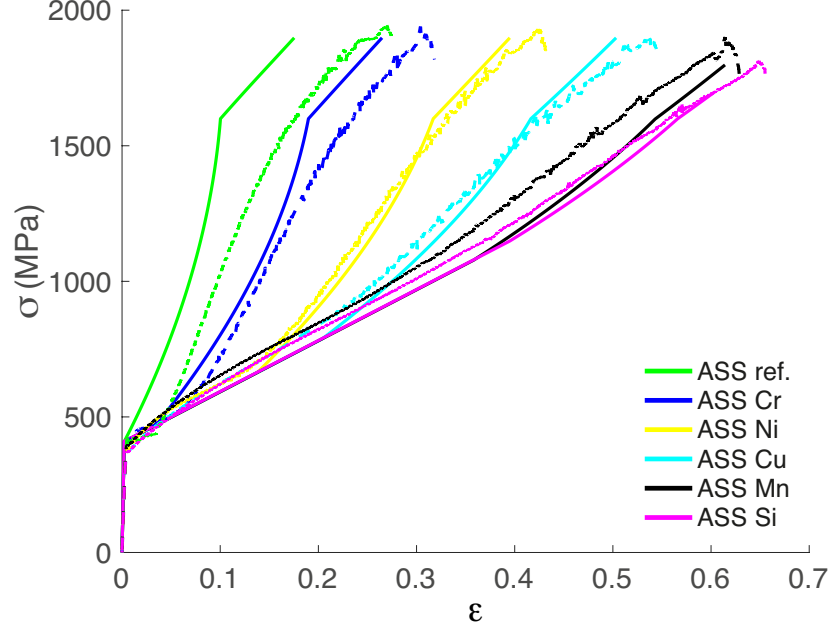


Figure 20: Stress/strain curves for all grades - experimental (dashed lines) vs. modeling results

Table 6: Martensite fraction threshold σ_s and strengthening θ_s parameters

Casts	ASS ref.	ASS Cr	ASS Ni	ASS Cu	ASS Mn	ASS Si
σ_s (MPa)	320	470	665	790	1080	1150
θ_s (MPa)	6842	4614	3636	2810	2345	2260

curve fitting allows the following equation to be proposed:

$$\sigma_s = a_1 Ms + a_2 \quad (39)$$

with $a_1 = -17.86 \text{ MPa}/^\circ\text{C}$ and $a_2 = 2314 \text{ MPa}$.

Figure 23 shows θ_s as a function of Ms . The following function has been used for the curve fitting. This function allows an asymptotic saturation at k_A (strengthening parameter of pure austenite) for low temperature.

$$\theta_s = k_A + a_3 \exp\left(\frac{Ms + a_4}{a_5}\right) \quad (40)$$

A least-square curve fitting allows the following parameters to be identified: $a_3 = 13.28 \text{ MPa}$, $a_4 = -248.2^\circ\text{C}$ and $a_5 = 18.31^\circ\text{C}$.

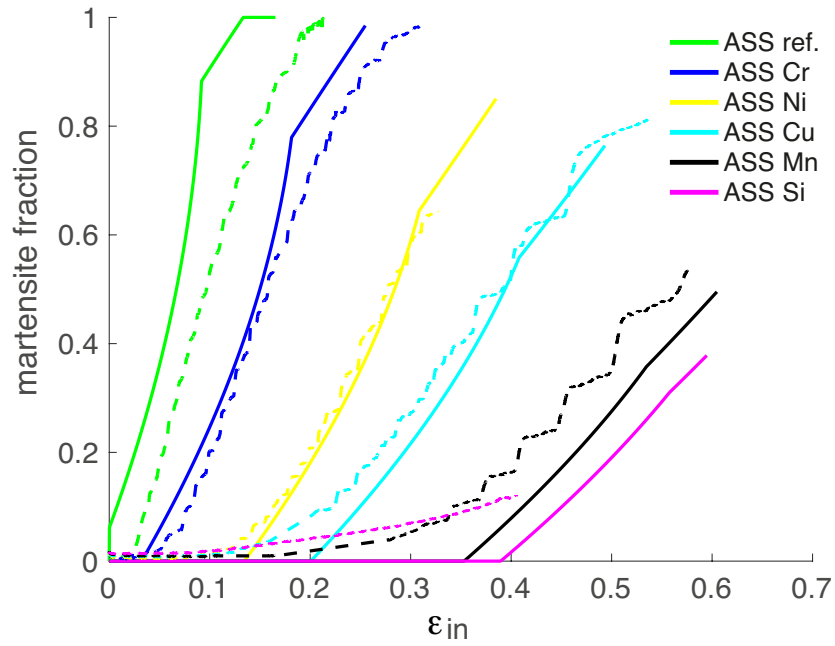


Figure 21: Martensite volume fraction as a function of inelastic strain for all grades - experimental (dashed lines) vs. modeling results

These new relationships complemented with M_s vs. composition equation (1) allow a theoretical evaluation of stress-strain and martensite fraction production for various stainless steel compositions (remaining in the same M_s range as the range of our results).

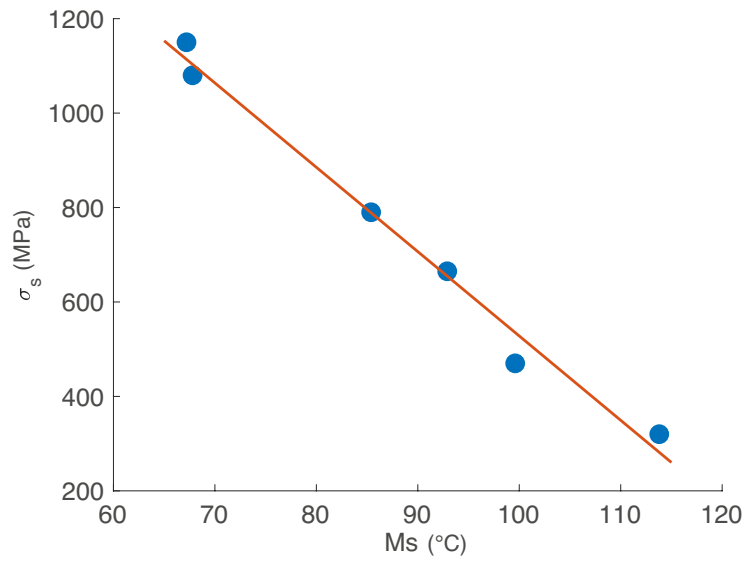


Figure 22: Transformation stress threshold σ_s as a function of martensite start temperature Ms.

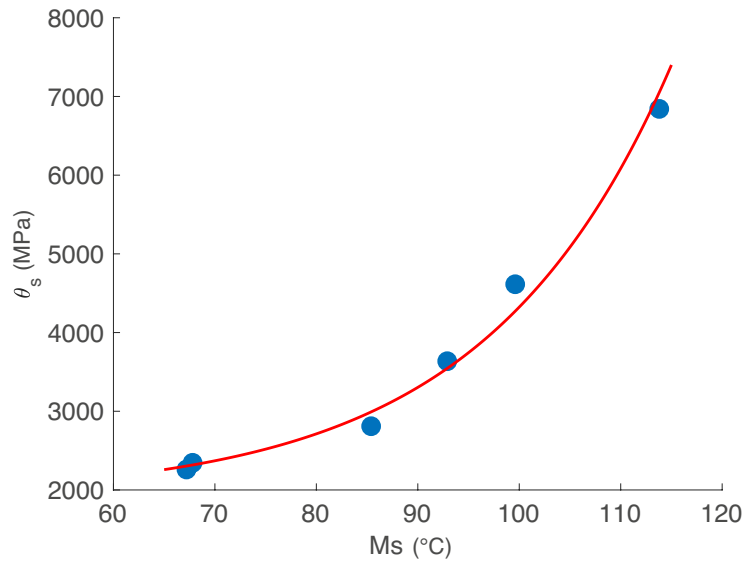


Figure 23: Austenite strengthening parameter θ_s as a function of martensite start temperature Ms.

5. Conclusion

The strain-induced martensitic transformation was studied in medium manganese austenitic stainless steels. Tensile tests at room temperature were carried out on six casts with different chemical compositions so that the stability of the austenite can be varied. The martensite transformation was followed by magnetic measurements during straining. Strain heterogeneities were analyzed by digital image correlation (DIC). The main results are:

- DIC measurements confirm the nucleation and propagation of a Lüders band immediately after the yield point for the most unstable samples (ASS ref. and ASS Cr). All grades deform by Portevin-le-Châtelier band propagation after a certain level of plastic deformation. The more stable is the sample, the higher the strain threshold.
- after a stress threshold which depends on the grade, the martensite fraction evolves linearly with the stress with a constant slope whatever the austenite stability.
- this linear relationship allows the development of a metallurgical/mechanical model that couples the austenite deformation with the martensite transformation. Depending on a single parameter that describes the austenite stability, M_s , the predicted stress-strain curves account for the most salient experimental results. The model remains however a simple *play* model that cannot be used without precaution in cyclic, multiaxial, or non-proportional situations.

Acknowledgements

The work was funded by **Aperam Stainless Steel Research Center, Isbergues, France**. The authors wish to thank Drs Francis Chassagne and Jean-Denis Mithieux for material preparation and provision, and useful discussions. The authors wish to thank Pr François Hild for his help regarding DIC questions and Mr Marc Bonnet for XRD measurements.

Data availability

The raw data required to reproduce these findings cannot be shared at this time as the data is also part of an ongoing study. The processed data required to reproduce these findings cannot be shared at this time as the data is also part of an ongoing study.

References

- [1] K. H. Lo, C. H. Shek, J. K. Lai, Recent developments in stainless steels, *Materials Science and Engineering R: Reports* 65 (4-6) (2009) 39–104.

- [2] P. Santacreu, C. Miraval, L. Faivre, P. Girardon, A. Acher, J. Herbelin, 'Back to the future' of stainless steel in the automotive - *in French*, MATEC Web of Conferences 7 (2013) 01001.
- [3] P. Mangonon Jr., G. Thomas, The martensite phases in 304 stainless steel, Metallurgical Transactions 1 (1970) 1577–1586.
- [4] J. Talonen, H. Hänninen, Formation of shear bands and strain-induced martensite during plastic deformation of metastable austenitic stainless steels, Acta Materialia 1 (2007) 6108–6118.
- [5] P. Haušild, V. Davydov, J. Drahokoupil, M. Landa, P. Pilvin, Characterization of strain-induced martensitic transformation in a metastable austenitic stainless steel, Materials and Design 31 (4) (2010) 1821–1827.
- [6] P. J. Jacques, S. Allain, O. Bouaziz, A. De, A.-F. Gourgues, B. Hance, Y. Houbaert, J. Huang, A. Iza-Mendia, S. Kruger, M. Radu, L. Samek, L. Speer, L. Zhao, S. van der Zwaag, On measurement of retained austenite in multiphase trip steels results of blind round robin test involving six different techniques, Materials Science and Technology 25 (2009) 567–574.
- [7] M. Moallemi, A. Kermanpur, A. Najafizadeh, A. Rezaee, H. Baghbadorani, P. Nezhadfar, Deformation-induced martensitic transformation in a 201 austenitic steel: The synergy of stacking fault energy and chemical driving force, Materials Science and Engineering A 653 (2016) 147–152.
- [8] B. Ennis, E. Jimenez-Melero, E. Atzema, M. Krugla, M. Azeem, D. Rowley, D. Daisenberger, D. Hanlon, P. Lee, Metastable austenite driven work-hardening behaviour in a trip-assisted dual phase steel, International Journal of Plasticity 88 (2017) 126–139.
- [9] T. Park, L. Hector, X. Hu, F. Abu-Farha, M. Fellingner, H. Kim, R. Esmaeilpour, F. Pourboghrat, Crystal plasticity modeling of 3rd generation multi-phase ahss with martensitic transformation, International Journal of Plasticity 120 (2019) 1–46.
- [10] M. Lamari, S. Allain, G. Geandier, J. Hell, A. Perlade, K. Zhu, In situ determination of phase stress states in an unstable medium manganese duplex steel studied by high-energy x-ray diffraction, Metals 10 (10) (2020).
- [11] L. Zhao, N. van Dijk, E. Bruck, J. Sietsma, S. van der Zwaag, Magnetic and x-ray diffraction measurements for the determination of retained austenite in trip steels, Materials Science and Engineering A 313 (2001) 145–152.
- [12] M. Callahan, O. Hubert, F. Hild, A. Perlade, J. H. Schmitt, Coincidence of strain-induced TRIP and propagative PLC bands in Medium Mn steels, Materials Science and Engineering A 704 (2017) 391–400.

- [13] Q. Long, Z. Zhu, X. Zhang, D. Li, Acoustic emission of martensitic transformation induced by strain during tensile testing in a fe-ni-c alloy, *Scripta Metallurgica and Materialia* 26 (1992) 1095–1100.
- [14] A. Beese, D. Mohr, Identification of the direction-dependency of the martensitic transformation in stainless steel using in situ magnetic permeability measurements, *Experimental Mechanics* 51 (2011) 667–676.
- [15] M. Radu, J. Valy, A. Gourgues, F. Le Strat, A. Pineau, Continuous magnetic method for quantitative monitoring of martensitic transformation in steels containing metastable austenite, *Scripta Materialia* 52 (2005) 525–530.
- [16] I. Souza Filho, M. Sandim, R. Cohen, L. Nagamine, J. Hoffmann, R. Bolmaro, H. Sandim, Effects of strain-induced martensite and its reversion on the magnetic properties of aisi 201 austenitic stainless steel, *Journal of Magnetism and Magnetic Materials* 419 (2016) 156–165.
- [17] M. Sandim, I. Souza Filho, C. Mota, K. Zilnyk, H. Sandim, Microstructural and magnetic characterization of a lean duplex steel: Strain-induced martensite formation and austenite reversion, *Journal of Magnetism and Magnetic Materials* 517 (2021) 167370.
- [18] E. Gorkunov, S. Zadvorkin, D. Mitropolskaya Vichuzhanin, K. Soloe'v, Change in magnetic properties of metastable austenite steel due to elasto-plastic deformation, *Metal Science and Heat Treatment* 51 (2009) 423–428.
- [19] J. Talonen, P. Aspegren, H. Hänninen, Comparison of different methods for measuring strain induced α -martensite content in austenitic steels, *Materials Science and Technology* 20 (2004) 1506–1512.
- [20] D. Jiles, Review of magnetic methods for nondestructive evaluation, *NDT International* 21 (1988) 311–319.
- [21] G. Dobmann, I. Altpeter, R. Becker, R. Kern, U. Laub, W. Theiner, Barkhausen noise measurements and related measurements in ferromagnetic materials, Djordjevic BB, Dos Reis H, editors, American Society for Nondestructive Testing., 1998.
- [22] M. Smaga, D. Eifler, Fatigue life calculation of metastable austenitic stainless steels on the basis of magnetic measurements, *Materials Testing* 51 (2009) 311–319.
- [23] K. Ishida, Calculation of the effect of alloying elements on the ms temperature in steels, *Journal of Alloys and Compounds* 220 (1995) 126–131.
- [24] C. Izawa, S. Wagner, M. Deutges, M. Martin, S. Weber, R. Pargeter, T. Michler, H. Uchida, R. Gemma, A. Pundt, Relationship between hydrogen embrittlement and md30 temperature: Prediction of low-nickel austenitic stainless steel's resistance, *International Journal of Hydrogen Energy* 44 (45) (2019) 25064–25075.

- [25] G. Meric de Bellefon, J. van Duysen, K. Sridharan, Composition-dependence of stacking fault energy in austenitic stainless steels through linear regression with random intercepts., *Journal of Nuclear Materials* (2017) 492.
- [26] L. Vitos, J. O. Nilsson, B. Johansson, Alloying effects on the stacking fault energy in austenitic stainless steels from first-principles theory, *Acta Materialia* 54 (14) (2006) 3821–3826. doi:10.1016/j.actamat.2006.04.013.
- [27] H. Leclerc, J. Neggers, F. Mathieu, F. Hild, S. Roux, Correli 3.0 iddn.fr.001.520008.000.s.p.2015.000.31500, Agence pour la Protection des Programmes, Paris (France) (2015).
- [28] P. Lacombe, G. Blanc, B. Baroux, G. Beranger, *Stainless Steels*, Les editions de Physique - Les Ulis (1993).
- [29] F. Hild, S. Roux, Comparison of local and global approaches to digital image correlation, *Experimental mechanics* 52 (2012) 1503–1519.
- [30] J.-E. Dufour, B. Beaubier, F. Hild, S. Roux, CAD-based displacement measurements with stereo-DIC To cite this version :, *Experimental Mechanics* 55 (2015) 1657–1668.
- [31] Z. Tomicevic, F. Hild, S. Roux, Mechanics-aided digital image correlation, *The Journal of Strain Analysis for Engineering Design* 48 (2013) 330–343.
- [32] O. Hubert, L. Daniel, Energetical and multiscale approaches for the definition of an equivalent stress for magneto-elastic couplings, *Journal of Magnetism and Magnetic Materials* 323 (13) (2011) 1766–1781. doi:10.1016/j.jmmm.2011.01.041.
- [33] C. Bormio-Nunes, O. Hubert, Piezomagnetic behavior of Fe-Al-B alloys, *Journal of Magnetism and Magnetic Materials* 393 (2015) 404–418. doi:10.1016/j.jmmm.2015.05.091.
- [34] O. Hubert, Multiscale magneto-elastic modeling of magnetic materials including isotropic second order stress effect, *Journal of Magnetism and Magnetic Materials* 491 (2019) 165564. doi:10.1016/j.jmmm.2019.165564.
- [35] O. Hubert, L. Daniel, L. Bernard, Multiscale modeling of magnetostrictive materials, *Encyclopedia of Smart Materials* 5 (2022) 337–354. doi:10.1016/B978-0-12-803581-8.12058-2.
- [36] L. Daniel, L. Bernard, O. Hubert, Multiscale Modeling of Magnetic Materials, *Encyclopedia of Smart Materials* 5 (2022) 32–49. doi:10.1016/b978-0-12-803581-8.12056-9.
- [37] Y. Li, W. Li, J. Hu, H. Song, X. Jin, Compatible strain evolution in two phases due to epsilon martensite transformation in duplex trip-assisted stainless steels with high hydrogen embrittlement resistance, *International Journal of Plasticity* 88 (2017) 53–69.

- [38] J. Voboril, V. Landa, P. Merinov, B. Beketov, Problems in the determination of ferrite content of austenitic steels, *Strojirenstvi* 29 (1979) 413–422.
- [39] L. Daniel, O. Hubert, R. Billardon, Homogenisation of magneto-elastic behaviour: from the grain to the macro scale, *Computational & Applied Mathematics* 23 (2004) 285–308.
- [40] L. Daniel, O. Hubert, N. Buiron, R. Billardon, Reversible magneto-elastic behavior: A multiscale approach, *Journal of the Mechanics and Physics of Solids* 56 (2008) 1018–1042.
- [41] A. Ouaddi, O. Hubert, J. Furtado, G. Gary, S. Depeyre, Piezomagnetic behavior: experimental observations and multiscale modeling, *Mechanics & Industry* 20 (810) (2020) 1–11. doi:10.1016/10.1051/meca/2020050.
- [42] R. Bozorth, *Ferromagnetism*, Van Nostrand, N.Y., 1951.
- [43] J. Makar, B. Tanner, The effect of stresses approaching and exceeding the yield point on the magnetic properties of high strength pearlitic steels, *NDT&E International* 31 (1998) 117–127.
- [44] O. Hubert, S. Lazreg, Two phase modeling of the influence of plastic strain on the magnetic and magnetostrictive behaviors of ferromagnetic materials, *Journal of Magnetism and Magnetic Materials* 424 (2017) 421–442.
- [45] G. Olson, M. Azrin, Transformation behavior of TRIP steels, *Metallurgical Transactions A* 9A (1978) 713–721.
- [46] B. Sun, N. Vanderesse, F. Fazeli, C. Scott, J. Chen, P. Bocher, M. Jahazi, S. Yue, Discontinuous strain-induced martensite transformation related to the portevin-le chatelier effect in a medium manganese steel, *Scripta Materialia* 133 (2017) 9–13.
- [47] M. Callahan, A. Perlade, J. Schmitt, Interactions of negative strain rate sensitivity, martensite transformation, and dynamic strain aging in 3rd generation advanced high-strength steels, *Material Sciences and Engineering A* 754 (2019) 140–151.
- [48] J. Wang, M. Huang, J. Hu, C. Wang, W. Xu, EBSD investigation of the crystallographic features of deformation-induced martensite in stainless steel, *Journal of Materials Science and Technology* 69 (2021) 148–155. doi:10.1016/j.jmst.2020.08.023.
- [49] G. B. Olson, M. Cohen, Kinetics of strain-induced martensitic nucleation, *Metallurgical Transactions A* 6 (4) (1975) 791–795. doi:10.1007/BF02672301.
- [50] R. Stringfellow, D. Parks, G. Olson, A constitutive model for transformation plasticity accompanying strain-induced martensitic transformations in metastable austenitic steels, *Acta Metallurgica and Materialia* 40 (1992) 1703–1716.

- [51] A. Ma, A. Hartmaier, A study of deformation and phase transformation coupling for trip-assisted steels, *International Journal of Plasticity* 64 (2015) 40–55.
- [52] Z. Feng, M. Zecevic, M. Knezevic, Stress-assisted ($\gamma \rightarrow \alpha'$) and strain-induced ($\gamma \rightarrow \epsilon \rightarrow \alpha'$) phase transformation kinetics laws implemented in a crystal plasticity model for predicting strain path sensitive deformation of austenitic steels, *International Journal of Plasticity* 136 (2021) 102807.
- [53] M.-G. Lee, S.-J. Kim, H. N. Han, Crystal plasticity finite element modeling of mechanically induced martensitic transformation (mimt) in metastable austenite, *International Journal of Plasticity* 26 (5) (2010) 688–710.
- [54] V. Levitas, D.-W. Lee, P. D.L., Interface propagation and microstructure evolution in phase field models of stress-induced martensitic phase transformations, *International Journal of Plasticity* 26 (3) (2010) 395–422.
- [55] S. Prüger, A. Seupel, M. Kuna, A thermomechanically coupled material model for trip-steel, *International Journal of Plasticity* 55 (2014) 182–197.
- [56] D. Connolly, C. Kohar, R. Mishra, K. Inal, A new coupled thermomechanical framework for modeling formability in transformation induced plasticity steels, *International Journal of Plasticity* 103 (2018) 39–66.
- [57] R. Ortwein, B. Skoczeń, J. Tock, Micromechanics based constitutive modeling of martensitic transformation in metastable materials subjected to torsion at cryogenic temperatures, *International Journal of Plasticity* 59 (2014) 152–179.
- [58] J. Lemaitre, J. Chaboche, *Mechanics of solid materials*, 1990.
- [59] K. Lavernhe-Taillard, S. Calloch, S. Arbab-Chirani, C. LExcellent, Multi-axial shape memory effect and superelasticity., *Strain* 45 (2009) 77–84.

Appendix A. Digital image correlation (DIC)

This appendix brings some comprehension elements about the DIC algorithm employed in this work. However, it does not substitute to some more detailed and accurate presentations available in [29–31].

Each image is first separated into local areas called *the region of interest* (ROI). The DIC algorithm assumes first that the grey level is conserved between the reference image $f(\mathbf{x})$ of the ROI at initial configuration (\mathbf{x} denoting a 2D position of a pixel) and a current image $g(\mathbf{x})$ at a deformed configuration, and that variations between images f and g are only due to the displacements $\mathbf{u}(\mathbf{x}, t)$. The displacement field solution of the problem minimizes the correlation residuals functions $\Phi^2(\mathbf{x})$ over the chosen ROI made of $m \times m$ pixels:

$$\Phi^2(\mathbf{x}) = \int_{ROI} [\phi(\mathbf{x})]^2 d\mathbf{x} = \int_{ROI} [g(\mathbf{x} + \mathbf{u}(\mathbf{x})) - f(\mathbf{x})]^2 d\mathbf{x} \quad (\text{A.1})$$

where $\phi(\mathbf{x}) = |g(\mathbf{x} + \mathbf{u}(\mathbf{x})) - f(\mathbf{x})|$ defines the field of correlation residuals. In Correli 3.0 software, the DIC problem resolution is ensured by the resolution of a Finite Element formulation (mesh illustrated in figure 2b). By adopting a global linear formulation, the residual field is integrated inside the ROI:

$$\mathbf{u}(\mathbf{x}) = \arg \min \int_{ROI} |g(\mathbf{x}) + \mathbf{grad}(g(\mathbf{x})) \cdot d\mathbf{u}^k - f(\mathbf{x})|^2 d\mathbf{x} \quad (\text{A.2})$$

where superscript k denotes the iteration index of the Newton procedure, and $\mathbf{u}(\mathbf{x})$ is spatially discretized using the spatial form functions φ_n and a_n the associated degrees of freedom:

$$\mathbf{u}(\mathbf{x}) = \sum_n a_n \varphi_n(\mathbf{x}) \quad (\text{A.3})$$

The resolution of the kinematic field $\mathbf{u}(\mathbf{x})$ is achieved by solving successively the following linear system:

$$\mathbf{M} \cdot d\mathbf{u} = \mathbf{b}$$

with

$$\mathbf{M} = M_{ij} \mathbf{e}_i \otimes \mathbf{e}_j$$

and

$$M_{ij} = \int_{ROI} (\varphi_i \cdot \mathbf{grad}(f(\mathbf{x}))) (\varphi_j \cdot \mathbf{grad}(f(\mathbf{x}))) d\mathbf{x} \quad (\text{A.4})$$

\mathbf{b} is a vector that vanishes when a perfect fit is obtained for each pixel.

Appendix B. Heat equation

The dissipation process must be complemented by the heat equation. We go back to the first principle:

$$\rho \dot{u} = \boldsymbol{\sigma} : \dot{\boldsymbol{\epsilon}} + q - \operatorname{div} \mathbf{q}^s \quad (\text{B.1})$$

and introduce

$$\dot{u} = \dot{\psi} + \dot{T}s + T\dot{s}$$

using again, on one hand, equation (22) and equation (28), on the other hand, we obtain:

$$\rho T \dot{s} = \sum_i f_i \boldsymbol{\sigma} : \dot{\boldsymbol{\epsilon}}_i^p + \sum_i f_i \boldsymbol{\sigma} : \dot{\boldsymbol{\epsilon}}_i^{tr} - \sum_i \rho \mathbf{g}_i \dot{f}_i + q - \operatorname{div} \mathbf{q}^s \quad (\text{B.2})$$

We consider s as a function of the same variable than ψ : $s(\epsilon^e, T, f_i)$:

$$\dot{s} = \frac{\partial s}{\partial \epsilon^e} : \dot{\boldsymbol{\epsilon}}^e + \frac{\partial s}{\partial T} \dot{T} + \sum_i \frac{\partial s}{\partial f_i} \dot{f}_i \quad (\text{B.3})$$

so that

$$\rho T \left(\frac{\partial s}{\partial \epsilon^e} : \dot{\boldsymbol{\epsilon}}^e + \frac{\partial s}{\partial T} \dot{T} + \sum_i \frac{\partial s}{\partial f_i} \dot{f}_i \right) = \sum_i f_i \boldsymbol{\sigma} : \dot{\boldsymbol{\epsilon}}_i^p + \sum_i f_i \boldsymbol{\sigma} : \dot{\boldsymbol{\epsilon}}_i^{tr} - \sum_i \rho \mathbf{g}_i \dot{f}_i + q - \operatorname{div} \mathbf{q}^s \quad (\text{B.4})$$

Considering next:

- thermoelasticity term

$$\rho T \frac{\partial s}{\partial \epsilon^e} : \dot{\boldsymbol{\epsilon}}^e = -\rho T \frac{\partial^2 \psi}{\partial T \partial \epsilon^e} : \dot{\boldsymbol{\epsilon}}^e = -\rho T \frac{\partial \boldsymbol{\sigma}}{\partial T} : \dot{\boldsymbol{\epsilon}}^e$$

- mixture law for specific entropy density as applied for specific free energy density

$$s = \sum_i f_i s_i$$

leading to:

$$\sum_i \frac{\partial s}{\partial f_i} \dot{f}_i = \sum_i s_i \dot{f}_i$$

- specific enthalpy density of phase i

$$h_i = \mathbf{g}_i + T s_i$$

- specific heat capacity at constant strain

$$\frac{\partial s}{\partial T} = \frac{c_\epsilon}{T}$$

The final expression of heat equation is obtained:

$$\rho c_\epsilon \dot{T} = \sum_i f_i \boldsymbol{\sigma} : \dot{\boldsymbol{\epsilon}}_i^p + \sum_i f_i \boldsymbol{\sigma} : \dot{\boldsymbol{\epsilon}}_i^{tr} - \sum_i \rho h_i \dot{f}_i + \rho T \frac{\partial \boldsymbol{\sigma}}{\partial T} : \dot{\boldsymbol{\epsilon}}^e + q - \text{div } \mathbf{q}^s \quad (\text{B.5})$$

The heat sources are the following:

- plastic strain
- transformation strain
- latent heat
- thermoelasticity

q denotes "other" sources (electromagnetic...), \mathbf{q}^s figures out the heat exchanges.